Instability regimes in flowing suspensions of swimming micro-organisms

Amir Alizadeh Pahlavan and David Saintillan[a)]
Department of Mechanical Science and Engineering, University of Illinois at Urbana-Champaign, Urbana, Illinois 61801, USA

(Received 31 August 2010; accepted 28 November 2010; published online 6 January 2011)

The effects of an external shear flow on the dynamics and pattern formation in a dilute suspension of swimming micro-organisms are investigated using a linear stability analysis and three-dimensional numerical simulations, based on the kinetic model previously developed by [D. Saintillan and M. J. Shelley, Phys. Fluids **20**, 123304 (2008)]. The external shear flow is found to damp the instabilities that occur in these suspensions by controlling the orientation of the particles. We demonstrate in our simulations that the rate of damping is direction-dependent: it is fastest in the flow direction, but slowest in the direction perpendicular to the shear plane. As a result, transitions from three- to two- to one-dimensional instabilities are observed to occur as shear rate increases, and above a certain shear rate the instabilities altogether disappear. The density patterns and complex flows that arise at long time in the suspensions are also analyzed from the numerical simulations using standard techniques from the literature on turbulent flows. The imposed shear flow is found to have an effect on both density patterns and flow structures, which typically align with the extensional axis of the external flow. The disturbance flows in the simulations are shown to exhibit similarities with turbulent flows, and in particular two of the seemingly universal characteristics of turbulent flows also occur, namely: (i) the bias of Q-R plots toward the second and fourth quadrants, corresponding to stable focus/stretching and unstable node/saddle/saddle flow topologies, respectively, and (ii) the alignment of the vorticity vector with the intermediate strain-rate eigenvector. However, the flows described herein also significantly differ from turbulent flows owing to the strong predominance of large scales, as exemplified by the very rapid decay of the kinetic energy spectrum, an effect further enhanced after the transitions to two- and one-dimensional instabilities. © *2011 American Institute of Physics*. [doi:10.1063/1.3529411]

I. INTRODUCTION

The emergence of large-scale density patterns and correlated flows in suspensions of self-propelled particles such as swimming micro-organisms[1–3] or artificial micro-swimmers[4–9] is a well-documented phenomenon that has received significant attention over the last decade.[10–12] These flows and patterns have been reported in a number of experiments,[13–21] where they have been shown to be characterized by large correlation lengths that greatly exceed the swimmer dimensions,[13–17] chaotic and intermittent dynamics exhibiting strong jets and vortices,[13,14] as well as enhanced swimmer and passive tracer diffusion.[18–20] These phenomena have also been reproduced in discrete particle simulations using various levels of approximation, including simple dipole models,[22,23] Stokesian dynamics simulations,[24,25] boundary integral methods,[26] and slender-body models.[27]

The effects described above are all consequences of the long-ranged hydrodynamic interactions that arise between the swimming particles in the Stokes flow regime. As a single particle propels itself through a viscous liquid, it exerts to leading order a force dipole on the surrounding fluid, which is a consequence of the balance between the equal and opposite thrust and drag forces resulting from propulsion.[22,28,29] With the exception of some unusual types of particles with perfect fore-aft symmetry, this dipole arises universally for all types of swimmers, the only distinguishing characteristic being its sign, which can be either positive or negative depending on the mechanism for swimming. Specifically, pusher particles, which exert a propulsive thrust near their tail, induce a negative force dipole, whereas puller particles, which exert a thrust near their head, induce a positive force dipole. In the far field, this dipole drives a disturbance flow that decays slowly as the inverse square separation distance from the particle center. When several particles are swimming together in a suspension, the superposition of all the disturbance flows they induce couples their motions in a nontrivial way, resulting in some cases in correlated dynamics as observed in experiments[13,14] and simulations.[23,27]

To elucidate the mechanisms leading to these correlated dynamics, several continuum models have been developed.[28–37] These models, going back to the seminal work of Aditi Simha and Ramaswamy,[28] couple evolution equations for the configuration of the suspension to the Navier–Stokes or Stokes equations for the fluid flow, via an effective coarse-grained stress tensor capturing the effect of the force dipoles exerted by the swimmers on wavelengths much longer than the characteristic particle size. In a recent study, Saintillan and Shelley[29,30] developed a kinetic theory based on a general Smoluchowski equation for the particle distribution function coupled to the Stokes equations for the macroscale flow driven by the dipoles due to swimming, and

[a)]Electronic mail: dstn@illinois.edu.

applied it to study the evolution of an initially homogeneous and isotropic suspension. Using a linear stability analysis, they uncovered a new instability occurring at long wavelengths in suspensions of pusher particles, which results in their local alignment at short times owing to mean-field hydrodynamic interactions. Such an instability does not arise for pullers. To investigate the long-time dynamics, they also performed two-dimensional nonlinear simulations of their kinetic equations, and showed that the instability also results in the growth of concentration fluctuations, in the form of dense patterns that form and break up repeatedly in time, accompanied by complex chaotic flows on the scale of the system size.

As most previous studies have focused on the behavior of these suspensions in quiescent liquids, little is known on the effects of an external flow on the pattern formation and dynamics in these systems. Such effects may play an important role in natural phenomena where micro-organisms often evolve in complex flow environments.[38–40] They are also directly relevant to the effective rheology of swimming particle suspensions, which have been shown to exhibit unusual and striking features such as decreased effective viscosities in pusher suspensions.[41] While these features have been explained theoretically using very simple models for isolated swimmers in an imposed flow,[42–47] the effects of hydrodynamic interactions and pattern formation have not been addressed and have remained completely unknown up to now.

The object of the present work is to investigate the effects of an externally imposed simple shear flow on the instabilities, dynamics, and pattern formation that are known to arise in suspensions of micro-organisms and have previously been characterized in quiescent environments. To this end, we extend the kinetic model developed by Saintillan and Shelley[29,30] in Sec. II to account for an external flow. This model is then used to perform a stability analysis in Sec. III, where we show that the imposed flow has a damping effect on the instability that occurs in quiescent suspensions. In Sec. IV, we complement the results from the stability analysis by fully nonlinear three-dimensional simulations of the kinetic equations. In the absence of shear, these simulations extend the two-dimensional simulations previously performed by Saintillan and Shelley.[29,30] When shear is applied, the simulations confirm the prediction of the stability analysis, and demonstrate that the rate of damping is direction-dependent and is strongest in the flow direction but slowest in the direction perpendicular to the shear plane. The characteristics of the three-dimensional density patterns and flow fields that arise are also analyzed in detail using techniques from the turbulent flow literature. We conclude in Sec. V.

II. KINETIC MODEL

A. Governing equations

Following the kinetic model previously developed by Saintillan and Shelley,[29,30] we represent the configuration of a suspension of swimming particles by means of a time-dependent probability distribution function $\Psi(\mathbf{x},\mathbf{p},t)$ for the particle center-of-mass position $\mathbf{x}$ and orientation vector $\mathbf{p}$, which has unit norm and describes the direction of swimming. This distribution function satisfies a Smoluchowski equation[48]

$$\frac{\partial \Psi}{\partial t} = -\nabla_x \cdot (\dot{\mathbf{x}}\Psi) - \nabla_p \cdot (\dot{\mathbf{p}}\Psi), \tag{1}$$

where ∇_p is the gradient operator on the surface of the unit sphere Ω and is defined as

$$\nabla_p = (\mathsf{I} - \mathbf{pp}) \cdot \frac{\partial}{\partial \mathbf{p}}. \tag{2}$$

The particle fluxes $\dot{\mathbf{x}}$ and $\dot{\mathbf{p}}$ in Eq. (1) are modeled as

$$\dot{\mathbf{x}} = U_0\mathbf{p} + \mathbf{v} - D\nabla_x(\ln \Psi), \tag{3}$$

$$\dot{\mathbf{p}} = (\mathsf{I} - \mathbf{pp}) \cdot \nabla_x \mathbf{v} \cdot \mathbf{p} - d\nabla_p(\ln \Psi). \tag{4}$$

In Eq. (3), the center-of-mass flux is expressed as the sum of three terms, accounting for particle swimming with velocity $U_0\mathbf{p}$, advection by the local fluid velocity $\mathbf{v}(\mathbf{x},t)$, and center-of-mass diffusion with isotropic diffusivity D, assumed to be constant. Similarly, Eq. (4) accounts for particle rotation under the effect of the local velocity gradient via Jeffery's equation,[49] where it is assumed that the particle has a high aspect ratio. Rotational diffusion is also included with constant diffusivity d. Note that the assumption of constant diffusivities should be viewed as an approximation, and that in a real system these diffusivities may depend on the orientation of the particles or on concentration for instance. Finally, the probability distribution function is normalized as

$$\frac{1}{V}\int_V d\mathbf{x} \int_\Omega d\mathbf{p}\Psi(\mathbf{x},\mathbf{p},t) = n. \tag{5}$$

Here, $V=L^3$ denotes the volume of the system and is assumed to be a cube of linear dimension L, and $n=N/V$ denotes the mean number density of the suspension, where N is the total number of swimming particles.

To close Eqs. (1), (3), and (4), the fluid velocity $\mathbf{v}$ and corresponding velocity gradient $\nabla_x\mathbf{v}$ must be determined. Here, we decompose the velocity as the sum of an imposed linear flow with uniform and constant velocity gradient A and of the disturbance velocity $\mathbf{u}$ induced by the particles as they swim:

$$\mathbf{v}(\mathbf{x},t) = \mathbf{x} \cdot \mathsf{A} + \mathbf{u}(\mathbf{x},t). \tag{6}$$

For a linear shear flow in the x-direction, the tensor A is expressed as $\mathsf{A}=S\hat{\mathbf{y}}\hat{\mathbf{x}}$, where S is the constant shear rate (see Fig. 1), and $\hat{\mathbf{x}}$ and $\hat{\mathbf{y}}$ denote unit vectors in the x- and y-directions. In the low-Reynolds-number regime relevant to the locomotion of micro-organisms, the disturbance fluid flow driven by the particles satisfies the Stokes equations:

$$\nabla_x q - \mu\nabla_x^2\mathbf{u} = \nabla_x \cdot \boldsymbol{\Sigma}^p, \quad \nabla_x \cdot \mathbf{u} = 0, \tag{7}$$

where μ is the dynamic viscosity of the suspending fluid, and q is the pressure. In Eq. (7), $\boldsymbol{\Sigma}^p(\mathbf{x},t)$ is the particle extra stress, obtained as the orientational average of the force dipoles $\mathsf{S}(\mathbf{p})$ exerted by the particles on the fluid[50,51]

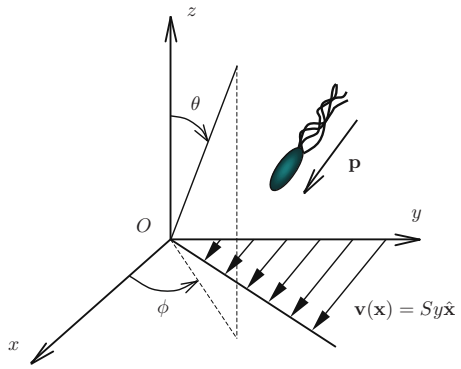

FIG. 1. (Color online) Problem geometry and coordinate system.

$$\mathbf{\Sigma}^p(\mathbf{x},t) = \int_\Omega \mathsf{S}(\mathbf{p})\Psi(\mathbf{x},\mathbf{p},t)d\mathbf{p}. \tag{8}$$

For a swimming particle in an external flow, the dipole $\mathsf{S}(\mathbf{p})$ arises from two contributions: resistance to stretching under the local flow, and self-propulsion. The dipole due to the external flow can be expressed as[52,53]

$$\mathsf{S}^f(\mathbf{p}) = C(\mathbf{pp}:\mathsf{A})\left(\mathbf{pp} - \frac{\mathsf{I}}{3}\right), \tag{9}$$

where the constant C depends on the particle shape; for a slender particle of inverse aspect ratio ε, it can be modeled using slender-body theory[52,53] as $C=\pi\mu l^3/6\ln(2/\varepsilon)$. Note that in all rigor, $\mathsf{S}^f(\mathbf{p})$ should also include a contribution from the disturbance velocity gradient $\nabla_x\mathbf{u}$. However, this contribution is of order $O(n^2)$ compared to order $O(n)$ for the contribution of the external flow, so we can safely neglect it in the limit of a dilute suspension. Finally, the permanent dipole resulting from self-propulsion can be expressed in the form

$$\mathsf{S}^s(\mathbf{p}) = \sigma_0\left(\mathbf{pp} - \frac{\mathsf{I}}{3}\right), \tag{10}$$

where the dipole strength σ_0 is a constant parameter whose sign depends on the mechanism for swimming. Head-actuated swimmers or pullers, such as the micro-alga *Chlamydomonas reinhardtii*, result in $\sigma_0>0$, whereas rear-actuated swimmers or pushers, such as most swimming bacteria including *Escherichia coli* and *Bacillus subtilis*, result in $\sigma_0<0$. In addition, it can be shown from dimensional analysis that σ_0 is related to the single-particle swimming speed U_0 and particle length l by a relation of the form $\sigma_0/\mu U_0 l^2=\alpha$, where α is a dimensionless $O(1)$ parameter with the same sign as σ_0.

Note that if the angular diffusivity d results from thermal fluctuations (Brownian rotations), an additional Brownian dipole also arises and is given by[45,46,48]

$$\mathsf{S}^b(\mathbf{p}) = kT\left(\mathbf{pp} - \frac{\mathsf{I}}{3}\right), \tag{11}$$

where kT is the thermal energy of the liquid. Note that S^b is formally identical to S^s [compare Eqs. (10) and (11)], so that including it simply offsets the value of σ_0 by kT. For typical micro-organisms such as bacteria and micro-algae, $kT \ll |\sigma_0|$, so we can neglect S^b compared to S^s in the following discussion. Note, however, that the Brownian dipole may be significant in suspensions of artificial micro-swimmers,[4–9] whose motions can be significantly affected by thermal fluctuations.

Before moving on, we also introduce the local concentration field $c(\mathbf{x},t)$ and local particle director field $\mathbf{n}(\mathbf{x},t)$ defined from the distribution function Ψ as

$$c(\mathbf{x},t) = \int_\Omega \Psi(\mathbf{x},\mathbf{p},t)d\mathbf{p}, \tag{12}$$

$$\mathbf{n}(\mathbf{x},t) = \frac{1}{c(\mathbf{x},t)}\int_\Omega \mathbf{p}\Psi(\mathbf{x},\mathbf{p},t)d\mathbf{p}. \tag{13}$$

Note that $c(\mathbf{x},t)=n$ and $\mathbf{n}(\mathbf{x},t)=\mathbf{0}$ in a uniform and isotropic suspension for which $\Psi(\mathbf{x},\mathbf{p},t)=n/4\pi$.

B. Nondimensionalization

In the following, we nondimensionalize the equations using the following characteristic length, velocity, and time scales: $l_c=(nl^2)^{-1}$, $u_c=U_0$, and $t_c=l_c/u_c=(U_0nl^2)^{-1}$. As noted by Saintillan and Shelley,[30] $l_c=(V/V_p)l$, where $V_p=Nl^3$ is the effective volume taken up by the N particles in the suspension. Upon nondimensionalization, the conservation Eq. (1) remains the same, but Ψ is now normalized as

$$\frac{1}{V^*}\int_V d\mathbf{x}\int_\Omega d\mathbf{p}\Psi(\mathbf{x},\mathbf{p},t) = 1, \tag{14}$$

where the dimensionless cell volume is $V^*=(L/l_c)^3=(nl^2L)^3$. The flux Eqs. (3) and (4) become

$$\dot{\mathbf{x}} = \mathbf{p} + \mathbf{v} - D^*\nabla_x(\ln\Psi), \tag{15}$$

$$\dot{\mathbf{p}} = (\mathsf{I}-\mathbf{pp})\cdot\nabla_x\mathbf{v}\cdot\mathbf{p} - d^*\nabla_p(\ln\Psi) \tag{16}$$

with dimensionless diffusion coefficients given by $D^*=Dnl^2/U_0$ and $d^*=d/U_0nl^2$. Finally, the dimensionless external shear rate is obtained as $S^*=S/U_0nl^2$, and the disturbance velocity satisfies the dimensionless Stokes equations in which the active particle stress tensor becomes

$$\mathbf{\Sigma}^p(\mathbf{x},t) = \alpha\int_\Omega \Psi(\mathbf{x},\mathbf{p},t)\left(\mathbf{pp} - \frac{\mathsf{I}}{3}\right)d\mathbf{p} + C^*\int_\Omega \Psi(\mathbf{x},\mathbf{p},t) \times(\mathbf{pp}:\mathsf{A}^*)\left(\mathbf{pp} - \frac{\mathsf{I}}{3}\right)d\mathbf{p} \tag{17}$$

with $\alpha=\sigma_0/\mu U_0 l^2$, $C^*=nC/\mu$, and $\mathsf{A}^*=S^*\hat{\mathbf{y}}\hat{\mathbf{x}}$. For a slender body, we also obtain $C^*=\pi nl^3/6\ln(2/\varepsilon)$. In particular, we see that C^* scales linearly with nl^3, which can be viewed as an effective volume fraction for the suspension,[48] and is much less than 1 in the limit of diluteness.

A few comments on the magnitude of these dimensionless parameters in actual biological systems are in order. Typical values of the dipole strength, swimming velocity, and particle dimensions for *Bacillus subtilis*, which is a bacterium commonly used in experiments, are given by Pedley:[37] $\sigma_0 \approx -2.7\times10^{-11}$ g cm^2 s^{-1},

$U_0 \approx 2\times 10^{-3}$ cm s^{-1}, $l \approx 4$ μm, and $\varepsilon \approx 0.2$. Based on these values, and assuming a typical bacterial density of 10^9 cells cm^{-3} (corresponding to a dilute volume fraction of approximately 0.2%), we obtain the following estimates for α and C^*:

$$\alpha \approx -0.84, \quad C^* \approx 0.014. \tag{18}$$

For the dimensionless shear rates considered in the rest of the paper (S^* of order 1 and less), we therefore see that active particle stresses, with magnitude α, will dominate the dissipative stresses due to the inextensibility of the particles, which have a typical magnitude of C^*S^* in Eq. (17). Based on this observation, the flow-induced stresses will be neglected in the stability analysis of Sec. III, though they will be included in the nonlinear simulations of Sec. IV. In the remainder of the paper, we exclusively use dimensionless variables, and omit asterisks (*) on all dimensionless parameters.

III. LINEAR STABILITY ANALYSIS

A. Eigenvalue problem

The stability of an isotropic homogeneous active suspension was previously investigated in the absence of an external flow ($S=0$) by Saintillan and Shelley[29,30] and Hohenegger and Shelley.[31] It was found that suspensions of pushers are subject to a long-wavelength instability below a given wave number k_c, whereas suspensions of pullers are stable for $k \le k_c$. Above k_c, both suspensions of pushers and pullers were found to be stable in the presence of rotational diffusion.[31] While the linear instability for pushers was found not to result in concentration fluctuations, numerical simulations[30] demonstrated that such fluctuations still appear at long time as a result of nonlinearities. In this section, we extend these previous studies to consider the effect of a nonzero external shear flow on the stability ($S \ge 0$).

In the base state, we take the distribution function $\Psi_0(\mathbf{p})$ to satisfy the following equation:

$$\nabla_p \cdot (\dot{\mathbf{p}}_0 \Psi_0) - d\nabla_p^2 \Psi_0 = 0, \tag{19}$$

where $\dot{\mathbf{p}}_0$ is given by

$$\dot{\mathbf{p}}_0 = (\mathsf{I} - \mathbf{pp}) \cdot \mathsf{A} \cdot \mathbf{p}. \tag{20}$$

For a linear shear flow, Eq. (19) must be solved numerically, for instance using finite differences,[54] or surface harmonic expansions.[46,55] Note that in the base state, Ψ_0 is uniform in space and therefore no disturbance flow occurs: $\mathbf{u}_0(\mathbf{x},t)=\mathbf{0}$, $q_0(\mathbf{x},t)=0$.

Next, we consider a small perturbation with respect to the uniform base state

$$\Psi(\mathbf{x},\mathbf{p},t) = \Psi_0(\mathbf{p}) + \epsilon \Psi_1(\mathbf{x},\mathbf{p},t), \tag{21}$$

where $\epsilon \ll 1$ and $|\Psi_1(\mathbf{x},\mathbf{p},t)| = O(1)$. This perturbation induces weak velocity and pressure fields

$$\mathbf{u}(\mathbf{x},t) = \epsilon \mathbf{u}_1(\mathbf{x},t), \quad q(\mathbf{x},t) = \epsilon q_1(\mathbf{x},t). \tag{22}$$

Substituting Eqs. (21) and (22) into the governing equations and linearizing in ϵ with respect to the base state, we obtain the following equation for Ψ_1:

$$\frac{\partial \Psi_1}{\partial t} + (\mathbf{p} + \mathbf{x}\cdot\mathsf{A}) \cdot \nabla_x \Psi_1 - 3(\mathbf{pp}:\mathsf{A})\Psi_1 - 3(\mathbf{pp}:\nabla_x \mathbf{u}_1)\Psi_0 + \dot{\mathbf{p}}_0 \cdot \nabla_p \Psi_1 + \dot{\mathbf{p}}_1 \cdot \nabla_p \Psi_0 - D\nabla_x^2 \Psi_1 - d\nabla_p^2 \Psi_1 = 0, \tag{23}$$

where $\dot{\mathbf{p}}_0$ is given by Eq. (20) and $\dot{\mathbf{p}}_1 = (\mathsf{I} - \mathbf{pp}) \cdot \nabla_x \mathbf{u}_1 \cdot \mathbf{p}$, and where we have used the two useful relations: $\nabla_p \cdot \dot{\mathbf{p}}_0 = -3\mathbf{pp}:\mathsf{A}$ and $\nabla_p \cdot \dot{\mathbf{p}}_1 = -3\mathbf{pp}:\nabla_x \mathbf{u}_1$, both easily derived from Jeffery's equation. To make further analytical progress, we assume a plane-wave perturbation with wave vector $\mathbf{k}$ for the distribution function. Because the imposed shear flow will advect and deform this plane wave, we write the distribution function as $\Psi_1(\mathbf{x},\mathbf{p},t) = \tilde{\Psi}(\mathbf{k},\mathbf{p})\exp[i\mathbf{k}\cdot(\mathbf{x}-\mathbf{x}\cdot\mathsf{A}t) + \sigma t]$, where the term involving the velocity gradient A accounts for deformation under shear and ensures that an initially periodic solution remains periodic as time goes on, and where σ is the complex growth rate which may *a priori* be a function of t. By linearity, similar forms can be assumed for all other perturbation variables. Plugging this form into Eq. (23) easily yields

$$(\sigma + k^2 D + i\mathbf{p}\cdot\mathbf{k} - 3\mathbf{pp}:\mathsf{A})\tilde{\Psi} - 3i(\mathbf{p}\cdot\mathbf{k})(\mathbf{p}\cdot\tilde{\mathbf{u}})\Psi_0 + \dot{\mathbf{p}}_0 \cdot \nabla_p \tilde{\Psi} + \tilde{\mathbf{p}} \cdot \nabla_p \Psi_0 - d\nabla_p^2 \tilde{\Psi} = 0, \tag{24}$$

where $k=|\mathbf{k}|$, and where we have substituted $t=0$ in order to focus on the evolution of the plane wave at the initial instant. In Eq. (24), the Fourier coefficient of the perturbation velocity is easily obtained as

$$\tilde{\mathbf{u}}(\mathbf{k}) = \frac{i}{k}(\mathsf{I} - \hat{\mathbf{k}}\hat{\mathbf{k}}) \cdot \tilde{\boldsymbol{\Sigma}}_p \cdot \hat{\mathbf{k}} \tag{25}$$

with $\hat{\mathbf{k}} = \mathbf{k}/k$ and

$$\tilde{\boldsymbol{\Sigma}}_p = \alpha \int_\Omega \tilde{\Psi}(\mathbf{k},\mathbf{p}) \left(\mathbf{pp} - \frac{\mathsf{I}}{3} \right) d\mathbf{p}. \tag{26}$$

In Eq. (26), we have only included the stress contribution from the permanent swimming dipoles, based on the observations of Sec. II B. The corresponding angular velocity in Eq. (24) is given by

$$\tilde{\mathbf{p}} = i(\tilde{\mathbf{u}}\cdot\mathbf{p})(\mathsf{I} - \mathbf{pp}) \cdot \mathbf{k}. \tag{27}$$

Equation (24), together with Eqs. (25)–(27), is an integro-differential equation, which constitutes an eigenvalue problem for the eigenfunction $\tilde{\Psi}(\mathbf{k},\mathbf{p})$ with eigenvalue σ. We solve it spectrally by expanding the eigenfunction on the basis of surface harmonics[56]

$$\tilde{\Psi}(\mathbf{k},\mathbf{p}) = \sum_{l,m} a_{lm}(\mathbf{k}) P_l^m(\cos\theta)\exp im\phi, \tag{28}$$

where the angles θ and ϕ parameterize the orientation vector $\mathbf{p}$ as (see Fig. 1)

$$\mathbf{p} = [\sin\theta\cos\phi, \sin\theta\sin\phi, \cos\theta] \tag{29}$$

and where $P_l^m(\cos\theta)$ denotes the associated Legendre polynomial of order (l,m). Substituting the expansion (28) into Eq. (24) yields, after very cumbersome algebra, a large-scale algebraic eigenvalue problem for the eigenvector of the co-

efficients $a_{lm}(\mathbf{k})$. This eigenvalue problem can be solved numerically using standard techniques, providing the complex eigenvalue σ and corresponding eigenfunction $\tilde{\Psi}(\mathbf{k},\mathbf{p})$ for a given wave vector $\mathbf{k}$.

B. Results

Because of the high complexity of the eigenvalue problem of Eq. (24) for an arbitrary wave vector $\mathbf{k}$, we limit our attention to the special case of a plane-wave perturbation in the direction normal to the shear plane: $\mathbf{k}=k\hat{\mathbf{z}}$. This has the advantage of greatly simplifying the eigenvalue problem, and we will also demonstrate in the numerical simulations of Sec. IV that the z-direction is in fact the most unstable direction. The eigenvalue problem can be solved for various choices of the diffusion coefficients D and d and of the shear rate S. As discussed by Saintillan and Shelley,[30] including translational diffusion D simply shifts the solution for $\mathrm{Re}(\sigma)$ by $-Dk^2$, resulting in a more rapid damping of the instabilities at high wave numbers. However, low wave numbers always remain unstable. On the other hand, the effects of rotational diffusion can be more subtle. In their recent analysis, Hohenegger and Shelley[31] showed that the growth of perturbations in suspensions of pusher particles is associated with a proliferation of oscillations in swimmer directions, and that rotational diffusion can therefore play an important role in stabilizing the flow at all spatial wavelengths. From a more practical standpoint, including rotational diffusion in the eigenvalue problem (24) also has the advantage of regularizing the eigenfunctions, which can otherwise become singular for some values of k,[30,31] thus allowing us to obtain meaningful solutions using only a finite number of surface harmonics. We therefore include rotational diffusion in all of our calculations, and we investigate the effects of both S and d on the growth rate σ.

Figure 2 shows the effect of the external shear rate S on the real and imaginary parts of σ, for a rotational diffusion coefficient of $d=0.01$. When there is no imposed flow ($S=0$), both $\mathrm{Re}(\sigma)$ and $\mathrm{Im}(\sigma)$ follow trends that are very similar to the previous results of Saintillan and Shelley[29,30] (which were technically obtained in the absence of rotational diffusion, $d=0$): at very low wave numbers, $\mathrm{Re}(\sigma)>0$ and $\mathrm{Im}(\sigma)=0$, suggesting that long-wavelength fluctuations will amplify exponentially at short times. At slightly higher values of k, $\mathrm{Im}(\sigma)$ becomes nonzero, indicating the existence of time oscillations in the dynamics at intermediate wave numbers. Above a critical wave number $k_c\approx 0.45$, the growth rate $\mathrm{Re}(\sigma)$ becomes negative so that all fluctuations are damped. In the absence of rotational diffusion, Saintillan and Shelley[30] had obtained a critical wave number $k_c\approx 0.55$.

As an imposed shear flow is applied ($S>0$), the solution to the dispersion relation becomes significantly more complex, with the emergence of unexpected branchings in the real part of the growth rate. The behavior of $\mathrm{Im}(\sigma)$ does not change significantly, although it becomes nonzero even at low wave numbers. The most noticeable trend is the decrease of the growth rate $\mathrm{Re}(\sigma)$ with S, as well as the reduction of the range of unstable wave numbers. This indicates a stabilizing effect by the external shear flow, and in fact any given positive wave number $k>0$ is found to ultimately become fully stable beyond a sufficiently large shear rate.

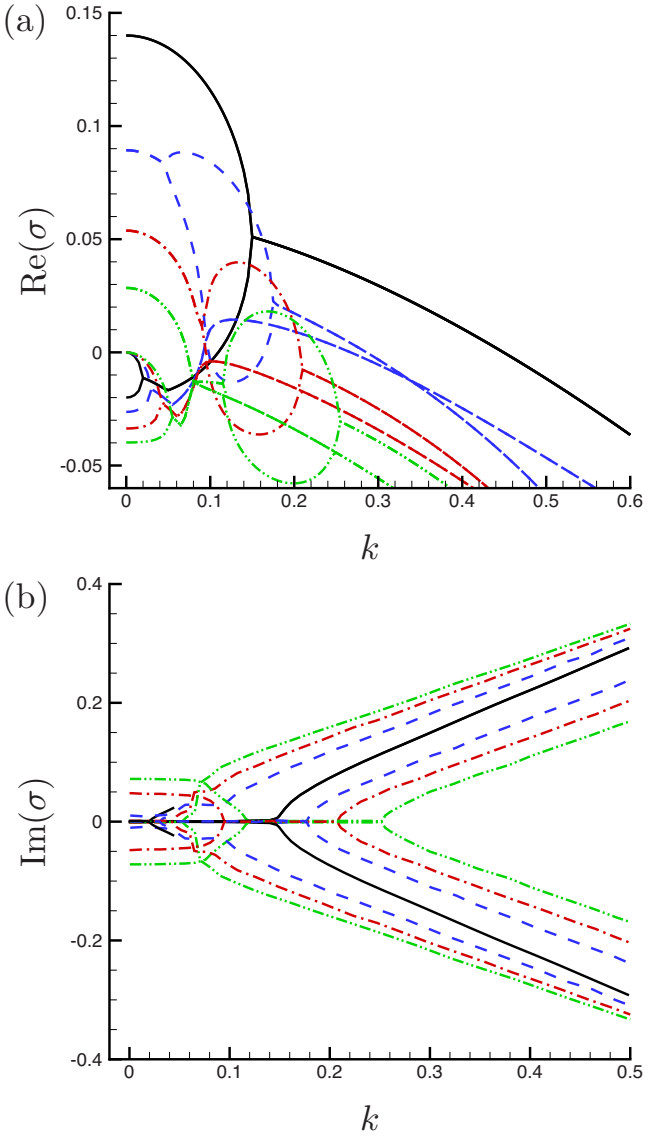

FIG. 2. (Color online) Effect of shear rate S on the (a) real part, and (b) imaginary part of the complex growth rate σ, for a rotational diffusion coefficient of $d=0.01$. $S=0$: solid line ——, $S=0.1$: dashed line ----, $S=0.2$: dash-dotted line –·–, and $S=0.3$: dash-dot-dotted line –··–.

The damping effect of the flow should not come as a surprise. Indeed, it has the effect of controlling particle orientations, as demonstrated in Fig. 3, showing the base state orientation distribution $\Psi_0(\mathbf{p})$ at two different shear rates (with a fixed rotational diffusivity of $d=0.01$). As expected and in agreement with previous studies,[46] the shear flow aligns particles along the x-axis, with a degree of alignment that increases with shear rate. Because the instability analyzed here is related to the local alignment of the particles via the active stress tensor $\boldsymbol{\Sigma}^p$ (which can be interpreted as a local nematic order parameter),[29,30,33] we expect this additional flow-induced alignment to hinder the growth of stress fluctuations associated with the instability.

The effects of rotational diffusion are analyzed in Fig. 4, showing the growth rate $\mathrm{Re}(\sigma)$ as a function of wave number k for two different values of d, with and without an external

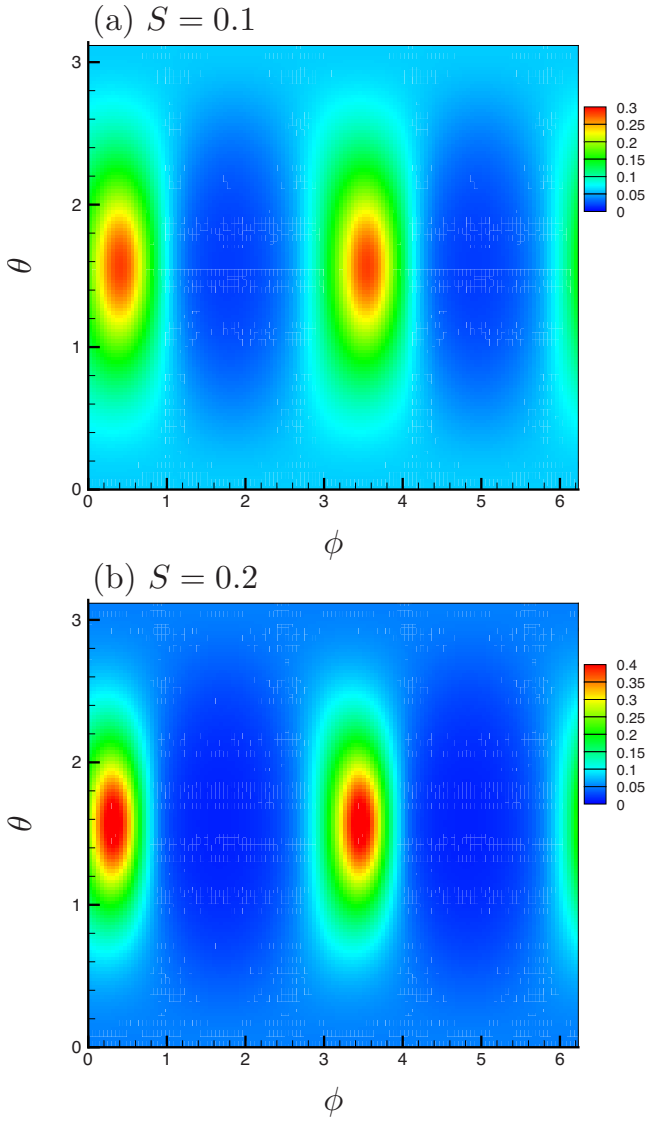

FIG. 3. (Color online) Base-state orientation distribution $\Psi_0(\mathbf{p})$, obtained by solution of Eq. (19), for $d=0.01$ and two different shear rates: (a) $S=0.1$ and (b) $S=0.2$.

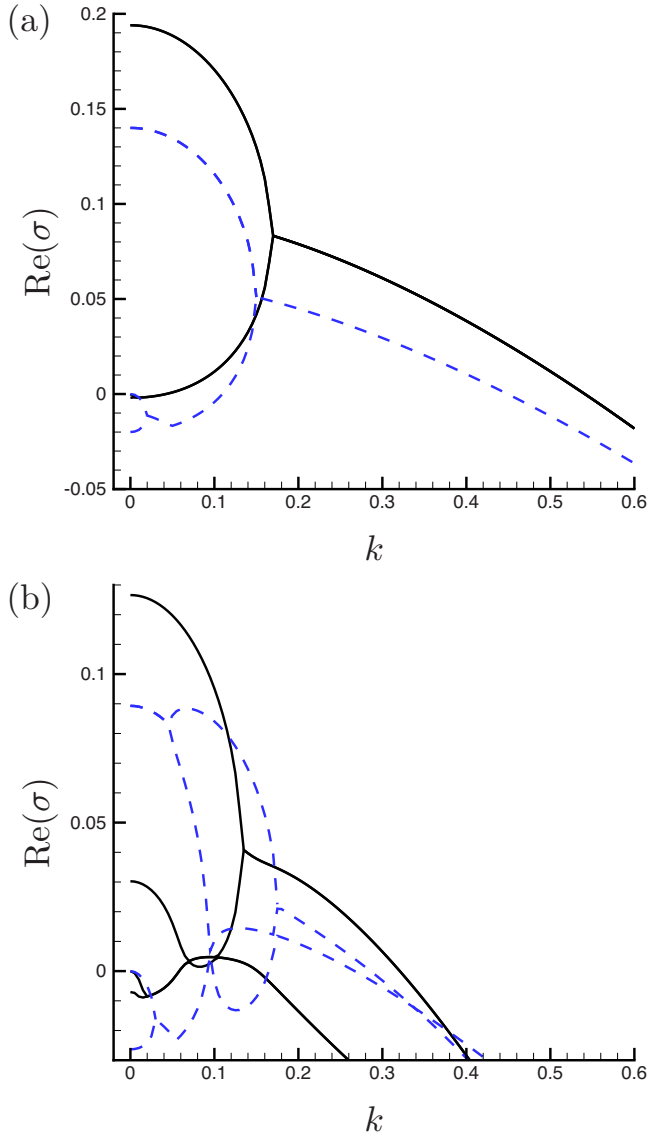

FIG. 4. (Color online) Effect of rotational diffusion coefficient d on the growth rate, or real part of σ, for (a) $S=0$ and (b) $S=0.1$. $d=0.001$: solid line ——, $d=0.01$: dashed line - - - - .

flow ($S=0$ and 0.1). We find that the effects of rotational diffusion on the growth rate are similar to those of shear: increasing d results in a damping of the instability as demonstrated by a lower growth rate and a reduction of the range of unstable wave numbers; additional complex branchings are also observed to appear in the solution of the dispersion relation. This stabilization can again be rationalized by the randomizing effect of diffusion on particle orientations, which again likely hinders the local alignment of the particles associated with the instability. This effect is also consistent with the previous theoretical observations of Hohenegger and Shelley.[31]

IV. NUMERICAL SIMULATIONS

A. Simulation method

To complement the predictions from the stability analysis of Sec. III, we now present results from three-dimensional numerical simulations of the kinetic equations described in Sec. II. Note that the kinetic model involves five independent variables in addition to time: three spatial coordinates x, y, and z, and two angles θ and ϕ for the parameterization of the orientation vector $\mathbf{p}$. This high dimensionality renders numerical solutions very expensive, and for this reason we developed a parallel scalable code, which was used in all the simulations. Typical grids of 128^3 points in space and 16^2 points for the orientation angles were used, corresponding to a total of more than half a billion grid points.

In order to use periodic boundary conditions for the solution of the flow equations, we employ Rogallo's method, in which the computational grid deforms to follow the mean imposed flow,[57,58] see Fig. 5. This method shares similarities with the classic Lees–Edwards boundary conditions[59] commonly used in particle simulations. Specifically, if x, y, and z denote spatial coordinates in a fixed reference frame, we define a new set of coordinates x', y', and z' in the deforming frame by

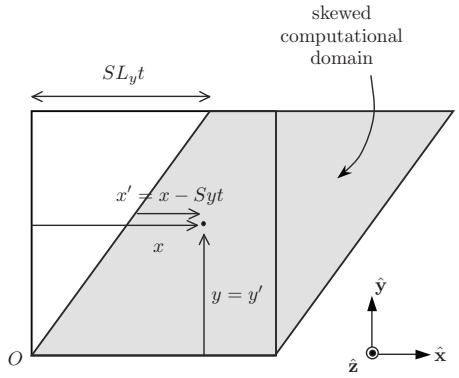

FIG. 5. Schematic illustrating the deformation of the computational domain with the mean imposed shear flow, after Rogallo (Ref. 57).

$$x' = x - Syt, \quad y' = y, \quad z' = z. \tag{30}$$

In this new coordinate system, a triply periodic field remains periodic as time progresses, allowing the use of Fourier-based methods. Specifically, the Stokes Eq. (7) is solved spectrally using truncated Fourier series expansions[60] and the fast Fourier transform algorithm. Knowing the disturbance velocity field **u**, we can then solve the conservation Eq. (1) for the distribution function Ψ using second-order finite differences for the fluxes, and a second-order Adams–Bashforth time-marching scheme.

As a result of the imposed shear, the computational grid introduced above becomes skewed as time increases. To allow the simulation to progress for a desirable amount of time without introducing large errors, it is necessary to perform a remeshing of the grid at regular time intervals.[57] The remeshing procedure makes use of the periodicity in the streamwise direction to move the data from the skewed grid onto a grid that is skewed in the opposite direction. In order to avoid data interpolation, this procedure is performed whenever $St=n(n+1)/2$ where n is a positive integer: at these times, grid points from the two skewed grids indeed exactly overlap.[57,58] With this method, the computational grid exactly matches the original orthogonal mesh whenever $St=2n$.

In all simulations, translational and rotational diffusion are both included to ensure that the solutions remain bounded over time (typical values of $D=d=0.01$ were used). All simulations shown are for pusher particles with $\alpha=-1$, as suspensions of pullers are known to be stable,[29,30] and we use a domain of linear size $L=50$ in all cases, which is large enough to ensure that instabilities occur in the absence of flow ($S=0$). The initial condition is taken to be a uniform isotropic suspension with a weak perturbation of the form

$$\Psi(\mathbf{x},\theta,\phi) = \frac{1}{4\pi} + \sum_i \epsilon_i \cos(\mathbf{k}_i \cdot \mathbf{x} + \xi_i) P_i(\theta) Q_i(\phi), \tag{31}$$

where $|\epsilon_i| \ll 1$ is a random coefficient of small magnitude, ξ_i is an arbitrary phase, and P_i and Q_i are low-order trigonometric polynomials in θ and ϕ with random coefficients. The initial random perturbations used in the simulations are band-limited, and typically only include the ten longest modes. It was indeed previously verified in two-dimensional simulations that including higher wave numbers in the initial distribution does not modify the long-time dynamics.[30]

B. Flow structures and velocity field characterization

At $t=0$, the initial distribution of Eq. (31) contains fluctuations at many length scales, and has a mean director field that is uncorrelated in space. As the simulations start, the evolution of the distribution function is characterized at short times by the decay of the imposed high-wave-number fluctuations. As time goes on, structures start to form on the scale of the computational domain. The magnitude of these fluctuations grows with time, and eventually reaches a statistical steady state as a result of a balance between the active input power generated by the particles and diffusive processes. At this stage, the structures in the flow are found to form, break up, and reorganize in a repeated and quasiperiodic fashion. These dynamics are qualitatively similar to those previously described by Saintillan and Shelley[29,30] in their two-dimensional simulations. Next, we characterize density fluctuations and fluid flow structures with emphasis on the effects of the external flow.

1. Density fluctuations

Figure 6 and accompanying online movie show the isosurfaces of the concentration field for different imposed shear rates S. When there is no shear flow [$S=0$, Fig. 6(a)], the concentration field is characterized by the formation of dense sheetlike structures, which form and break up in time but do not exhibit any preferred direction. These structures are the three-dimensional analogs of the concentration bands that were previously reported in two-dimensional simulations.[29,30] When a weak shear flow is imposed [$S=0.1$, Fig. 6(b)], the magnitude of the density fluctuations is observed to decay slightly, but three-dimensional structures are still observed to form. These structures are now affected by the external flow and are seen to align roughly along a 45° axis with respect to the flow direction, which corresponds to the axis of maximum extension of the external flow. As the shear rate increases further [$S=0.14$, Fig. 6(c)], a transition is found to occur, in which the concentration field becomes uniform in the flow direction (x-direction). Density fluctuations, however, can still be observed in the plane normal to the flow direction (y-z plane), and exhibit two-dimensional patterns that are qualitatively reminiscent of those observed in the previous two-dimensional simulations of Saintillan and Shelley.[29,30] In three dimensions, the particles therefore organize into tube-like structures that are perfectly aligned with the flow direction [Fig. 6(c)]. As the external flow becomes stronger [$S=0.2$, Fig. 6(d)], another transition is observed, by which the density field becomes uniform in both the x- and y-directions, with fluctuations only in the z-direction (direction perpendicular to the shear plane). In this case, the resulting concentration sheets [Fig. 6(d)] do not merge and break up, but instead travel past each other in the y-direction. Closer inspection indeed shows that the velocity field in this case consists of jets of fluid flowing up or down in the y-direction, with no velocity component in the z-direction

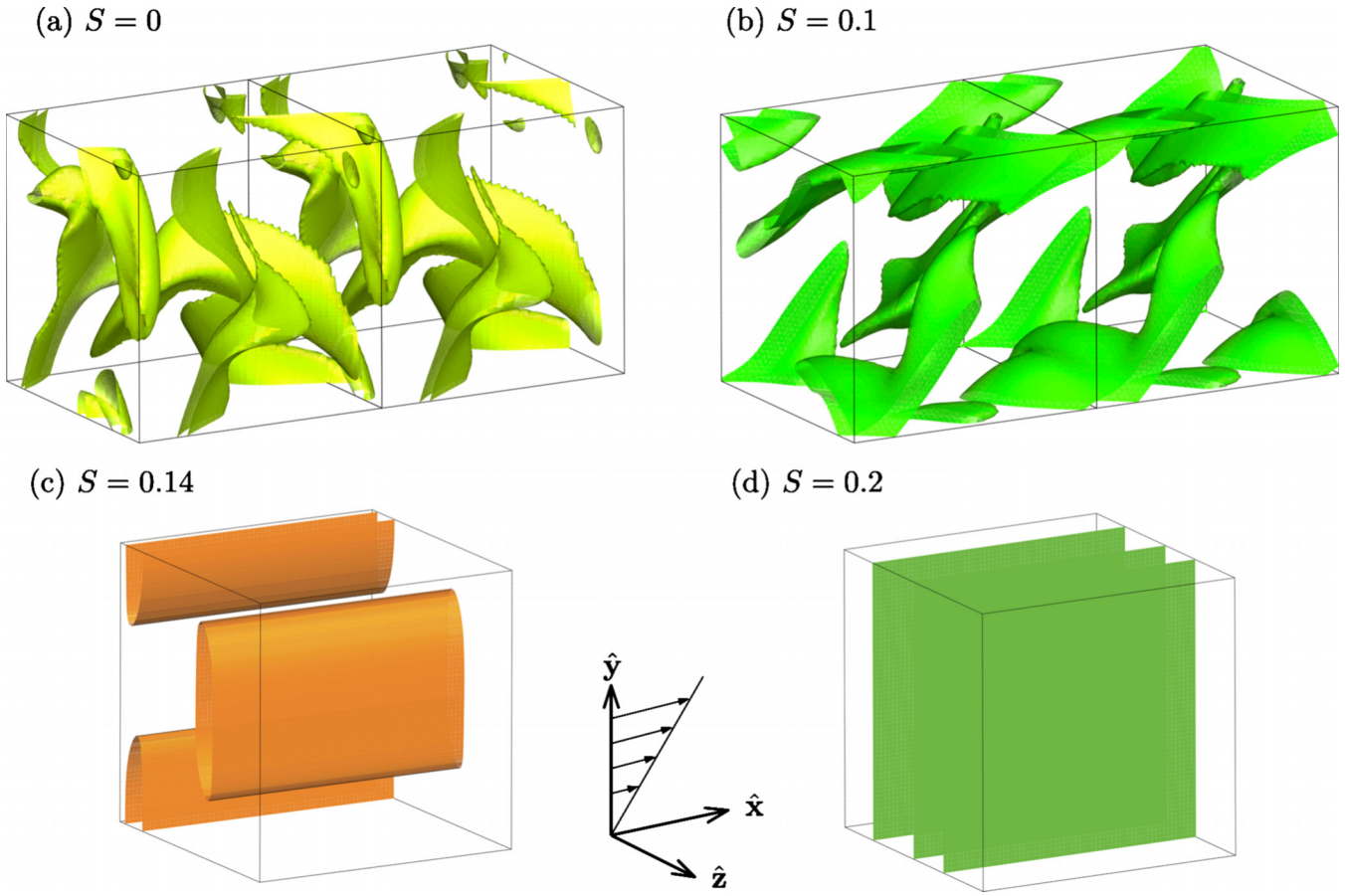

FIG. 6. (Color online) Concentration field isosurfaces for different shear rates: (a) $S=0$ at $c=1.5$, (b) $S=0.1$ at $c=1.2$, (c) $S=0.14$ at $c=1.1$, and (d) $S=0.2$ at $c=1$ (enhanced online). [URL: http://dx.doi.org/10.1063/1.3529411.1]

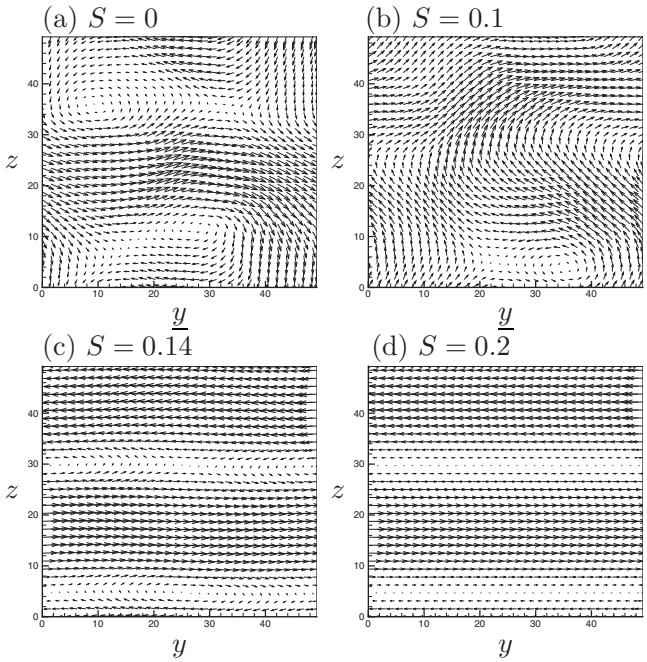

FIG. 7. Sample disturbance velocity fields in the y-z plane for different shear rates: (a) $S=0$ (no imposed shear flow), (b) $S=0.1$, (c) $S=0.14$, and (d) $S=0.2$.

[see Fig. 7(d)]. Finally, as the shear rate increases yet further ($S \gtrsim 0.3$), fluctuations in the z-direction are suppressed as well, resulting in a complete stabilization of the suspension, which becomes perfectly homogeneous in space. The observed transitions from three- to two- to one-dimensional dynamics as shear rate increases suggest that the rate of damping of the instabilities by the external flow is in fact direction-dependent: the z-direction, which the stability analysis of Sec. III B focused on, is seen to be the most unstable direction, followed by the y- and eventually x-directions.

2. Velocity fields

Associated with the density fluctuations described above are complex flow fields, which are illustrated in Fig. 7, showing sample disturbance velocity fields in the two-dimensional y-z plane. At low shear rates [$S=0$ and 0.1, Figs. 7(a) and 7(b)], the flow fields are three-dimensional and chaotic, and characterized by complex flow patterns involving vortices and jets, in agreement with previous experimental observations.[13,14] These flow fields are also qualitatively similar to those previously obtained in two-dimensional continuum simulations,[29,30] and three-dimensional particle simulations.[22,23,27] Note that the flow fields, while chaotic and random, are very smooth and dominated by motions on the scale of the simulation box; this will be further discussed

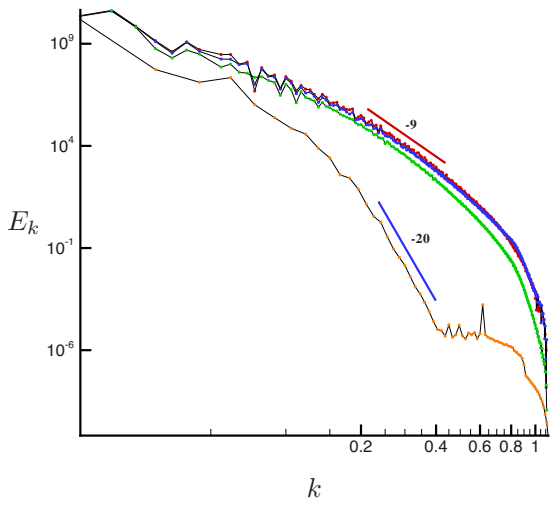

FIG. 8. (Color online) Kinetic energy spectrum for different shear rates: from top to bottom, $S=0$, $S=0.05$, $S=0.1$, and $S=0.14$.

below. As shear rate increases and the transition from three- to two-dimensional pattern formation takes place, the disturbance flow fields also become two-dimensional and exhibit fluid jets separated by shear layers and vortices [$S=0.14$, Fig. 7(c)]. Eventually, the disturbance field becomes fully unidirectional [$S=0.2$, Fig. 7(d)] and is characterized by shear layers that contain the dense particle sheets previously observed in the concentration field in Fig. 6(d).

While the observed flow fields are chaotic and reminiscent of high-Reynolds-number turbulence (and we will indeed show below that both types of flows share similarities), they also differ significantly owing to the strong predominance of large scales in the present simulations, e.g., see Fig. 7(a). This can be further quantified by considering the kinetic energy spectrum, which is shown in Fig. 8. At low shear rates (i.e., before the transition to two-dimensional pattern formation), the energy spectrum E_k is found to decay with wave number k as k^{-9}. This very rapid decay can be compared to $k^{-5/3}$ for the kinetic energy spectrum in three-dimensional turbulence, and clearly demonstrates that the flows in suspensions of swimming micro-organisms are very smooth and strongly dominated by large scales. This becomes yet more striking after the transition to two-dimensional instabilities, when a power-law decay of k^{-20} is obtained (which can be compared to k^{-3} for two-dimensional turbulence). For a given instability regime, we find that the decay exponent does not depend on system size (although the magnitude of the spectrum does). Note that the exponent of -9 found here in the three-dimensional case differs from the exponent of -3.5 recently obtained by Saintillan and Shelley[61] using direct particle simulations: this discrepancy may be attributed to the presence of small-scale flows scaling on the size of the swimmers in the particle simulations, which are neglected in the present mean-field theory where only macroscale flows occurring at long wavelengths with respect to the swimmer dimensions are modeled.

3. Vortical structures

To further analyze the nature of the flow fields that arise in the suspensions, we proceed to describe the vortical structures in the flows. To this end, we make use of the Q-criterion of Hunt *et al.*,[62] which is based on the characterization of the local flow topology in terms of critical points.[63] Specifically, given a flow field $\mathbf{u}(\mathbf{x},t)$, the local nature of the flow at a given time and point in space can be characterized by the eigenvalues of the velocity gradient $\mathsf{A}=\nabla\mathbf{u}=\mathsf{E}+\mathsf{W}$, where E and W are the rate-of-strain and rate-of-rotation tensors, respectively. These eigenvalues satisfy the characteristic equation

$$\lambda^3 + P\lambda^2 + Q\lambda + R = 0, \tag{32}$$

where P, Q, and R are the invariants of the velocity gradient tensor. In the case of an incompressible flow, they are expressed as

$$P = -E_{ii} = 0, \tag{33}$$

$$Q = -(E_{ij}E_{ji} + W_{ij}W_{ji})/2, \tag{34}$$

$$R = -(E_{ij}E_{jk}E_{ki} + 3W_{ij}W_{jk}W_{ki})/3. \tag{35}$$

Because $P=0$ owing to incompressibility, we see that the local geometry of the flow is fully characterized by the second and third invariants. Noting that the definition (34) of the second invariant may also be written as

$$Q = (\|\mathsf{W}\|^2 - \|\mathsf{E}\|^2)/2, \tag{36}$$

where $\|\mathsf{W}\|^2=W_{ij}W_{ij}$ and $\|\mathsf{E}\|^2=E_{ij}E_{ij}$, we see that Q quantifies the local balance between shear strain and vorticity magnitude. Points in space with $Q>0$ can therefore be regarded as dominated by vorticity, whereas those with $Q<0$ are dominated by strain.[62,64]

Q-isosurfaces therefore provide a simple way of identifying vortical structures in the flow. These isosurfaces are shown in Fig. 9 for different shear rates. In good qualitative agreement with the observations made on Fig. 6, the vortical structures appear to be random and isotropic in the absence of shear flow [$S=0$, Fig. 9(a)], but become aligned with the axis of maximum extension of the external flow at intermediate shear rates [$S=0.1$, Fig. 9(b)]. Beyond the transition to two-dimensional instabilities, the vortical structures take the form of vortex tubes that are perfectly aligned in the flow direction and cause fluid rotation in the plane perpendicular to the flow [$S=0.14$, Fig. 9(c)]; these vortex tubes are found to coincide approximately with the position of the denser regions in the suspensions [compare Figs. 6(c) and 9(c)]. After the transition to one-dimensional instabilities, no vortical structures are present in the flow (not shown).

4. Q-R plots

More detailed information about the flows is also provided by the joint probability distribution of the second and third invariants Q and R. In the Q-R plane, the nature of the eigenvalues of the velocity gradient tensor can be determined by the value of the discriminant

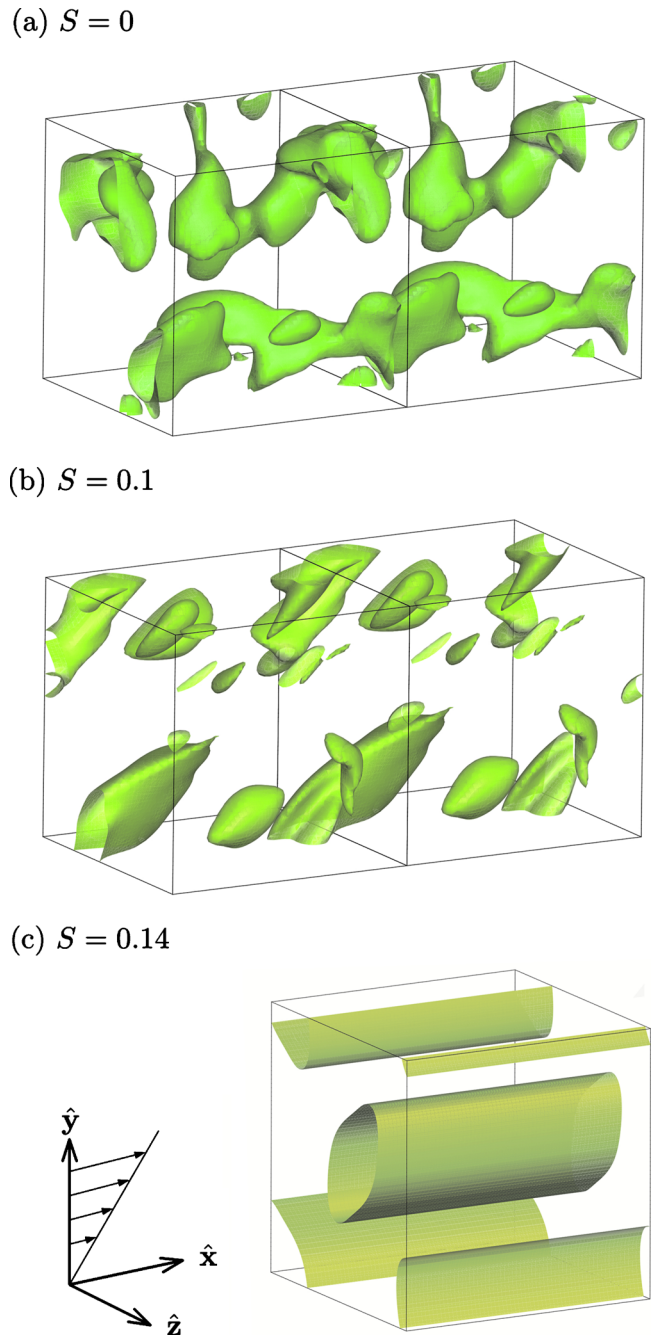

FIG. 9. (Color online) Vortical structures, identified by isosurfaces of the second invariant Q of the velocity gradient tensor [Eq. (36)], for different imposed shear rates: (a) $S=0$ at $Q=0.015$, (b) $S=0.1$ at $Q=0.0075$, and (c) $S=0.14$ at $Q=0.001$ (enhanced online). [URL: http://dx.doi.org/10.1063/1.3529411.2]

$$D = (27/4)R^2 + Q^3 \tag{37}$$

which defines the transition between straining and rotational flows. Specifically, a positive discriminant $D>0$ corresponds to one real and two complex conjugate eigenvalues, i.e., a rotational flow, whereas negative values of D correspond to three distinct real eigenvalues, i.e., a flow with no rotation. The curve $D=0$ corresponds to the case of three real eigenvalues in which two are equal (uniaxial compressional or extensional flow). The sign of the third invariant R provides information on the stability of the flow: if $R<0$, the real part

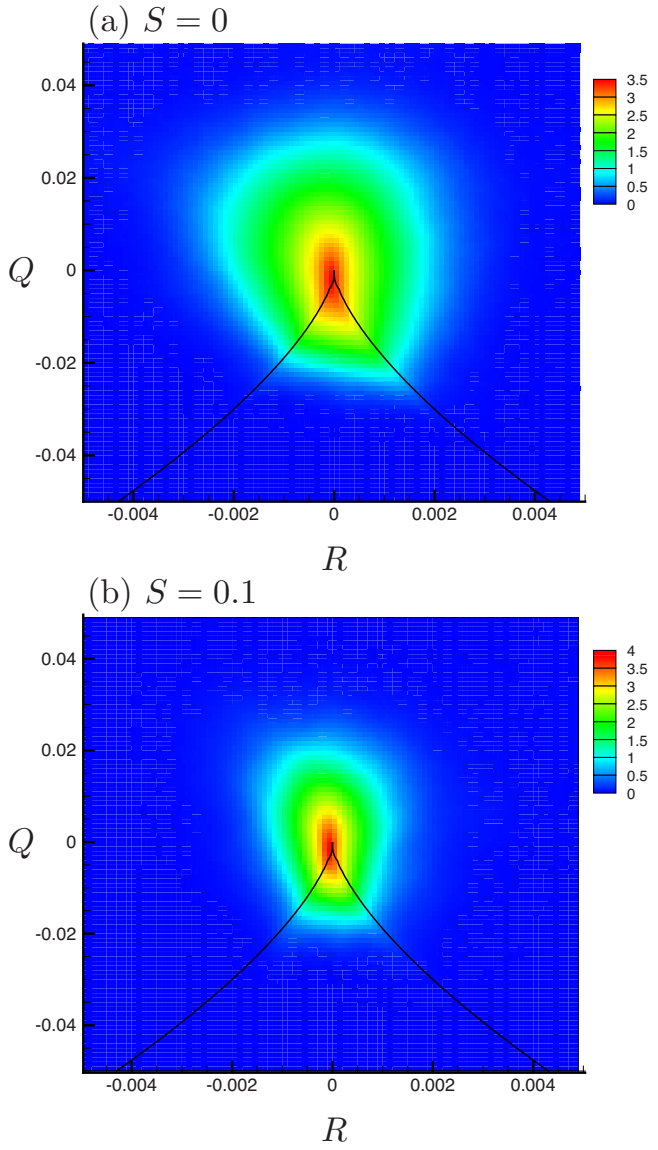

FIG. 10. (Color online) Q-R plots for different shear rates: (a) $S=0$ (no shear flow) and (b) $S=0.1$. In both plots, the black curves correspond to $D=0$, i.e., uniaxial extensional (left) and compressional (right) flows.

of two of the eigenvalues is negative, corresponding to a stable critical point, whereas $R>0$ indicates a positive real part for two of the eigenvalues and corresponds to an unstable critical point.[65]

Figure 10 shows two Q-R plots obtained from our simulations in the absence of shear ($S=0$) and with a weak shear flow ($S=0.1$). When there is no imposed flow [$S=0$, Fig. 10(a)], the diagram shows a shape similar to a tear drop along the second and fourth quadrants, which is repeatedly observed in turbulent flows and is often considered a universal characteristic of small scale turbulent motions.[65–68] Note, however, that the Q and R distributions in Fig. 10 are strongly concentrated near the origin, which indicates that the flows are strongly dominated by large-scale motions, unlike turbulent flows where small-scale motions also play an essential role. This observation is consistent with the previous discussion on the decay of the kinetic energy spectrum (Fig. 8). As a shear flow is imposed [$S=0.1$, Fig. 10(b)], the

shape of the Q-R plot remains essentially the same, but small-scale flows are further suppressed as shown by the more compact range of the Q and R distributions. In both cases, the Q-R plots show a slight tendency toward the second and fourth quadrants (owing to the tear-drop shape), which correspond to stable focus/stretching and unstable node/saddle/saddle flow topologies, respectively.[63] This tendency is slightly less pronounced when a flow is applied (S=0.1).

C. Joint probability distribution functions

To investigate the spatial orientation and alignment of the density and flow structures, we present results on the joint probability distribution functions (JPDFs) of various flow quantities in the (θ,ϕ) plane, where the angles θ and ϕ are defined in Fig. 1. In particular, the angle pairs $(\theta,\phi)=(\pi/2,0)$ and $(\pi/2,\pi)$ correspond to the direction of the imposed flow. Note that in order to eliminate the natural bias of the distributions toward the equator in spherical coordinates, we present the JPDFs in terms of cos θ and ϕ instead of θ and ϕ, in which case $(\cos\theta,\phi)=(0,0)$ and $(0,\pi)$ correspond to the flow direction. All the JPDFs shown below are averaged over space and time after a statistical steady state has been reached in the simulations.

Figure 11 shows the JPDFs of the concentration gradient vector ∇c, which provides information about the orientation of the density patterns. When no shear flow is applied [S=0, Fig. 11(a)], the probability distribution function is almost uniform (note the small range of the color map), with small fluctuations which can be attributed to noise and to the cubic geometry of the simulation domain. This confirms that the density patterns have no preferred direction when no flow is applied, as previously noted on Fig. 6(a). For low shear rates [S=0.1, Fig. 11(b)], the distribution becomes strongly anisotropic, with concentration gradients aligned preferentially along directions slightly above $\phi=3\pi/4$ and $\pi+3\pi/4$, and symmetric with respect to the shear plane $\theta=\pi/2$. This is consistent with density patterns roughly aligned with the $\phi=\pi/4$ and $\pi+\pi/4$ directions, in agreement with the shape of the isosurfaces in Fig. 6(b). After the instabilities becomes two-dimensional [S=0.14, Fig. 11(c)], the concentration gradients display two peaks at $\phi=\pi/2$ and $3\pi/2$, corresponding to a density field that is uniform in the flow direction ($\phi=0,\pi$) as seen in Fig. 6(c). Also note that the gradient distribution is biased toward $\theta=0$ and π (i.e., the z-axis), and this trend becomes clearer above the transition to the one-dimensional instability case (S=0.2, not shown), where all the gradients occur in the direction perpendicular to the shear plane [see Fig. 6(d)]. As the shear rate increases from 0 to 0.2, the characteristic magnitude of the concentration gradients is seen to increase (see color bars in Fig. 11), which indicates that the density patterns become increasingly sharp in stronger flows.

The JPDFs for the vorticity vector are shown in Fig. 12. As for the concentration gradient, the distribution is nearly isotropic when no shear flow is applied [S=0, Fig. 12(a)]. In a weak shear flow [S=0.1, Fig. 12(b)], the vorticity is found to align with the flow direction ($\phi\gtrsim 0$ and π, $\theta=\pi/2$), and

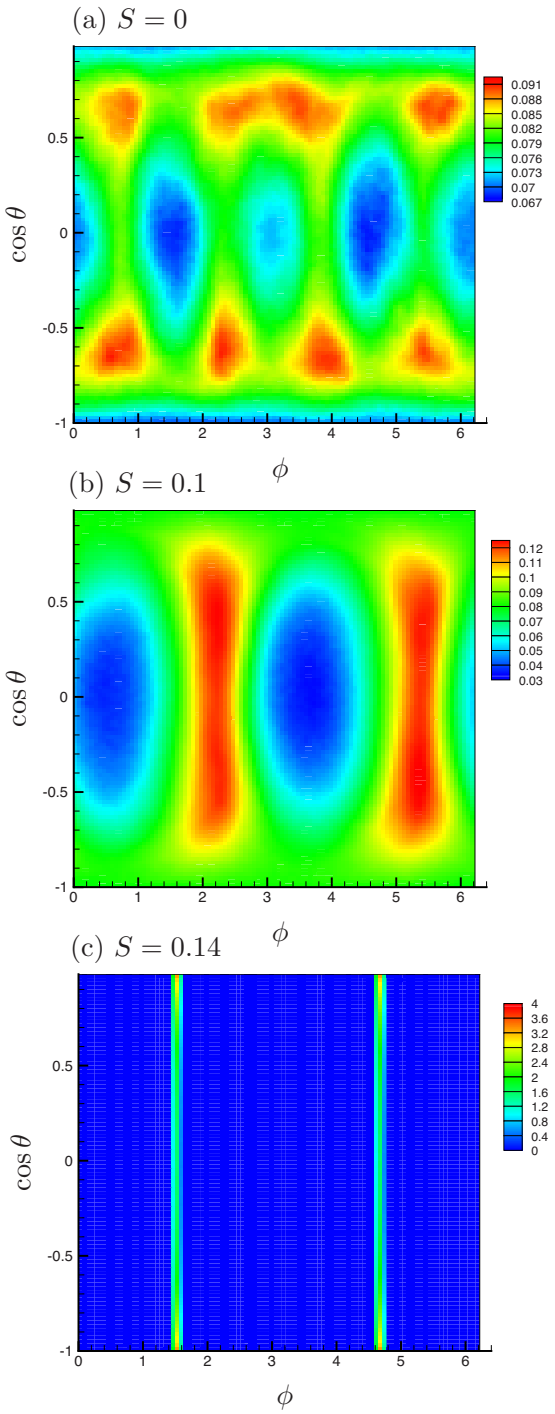

FIG. 11. (Color online) JPDF of the concentration gradient vector ∇c for different shear rates: (a) S=0 (no imposed flow), (b) S=0.1, and (c) S=0.14.

the peaks in the distribution correlate with the valleys in the JPDF of the concentration gradient [Fig. 11(b)]. This remains the case in the two-dimensional instability case [S=0.14, Fig. 12(b)], where the vorticity is found to be almost perfectly aligned with the flow direction. This suggests that vorticity tends to align with the density patterns; this is particularly clear in the two-dimensional instability case where vortex tubes in the flow direction directly correlate with the dense regions in the flow [for instance, compare Figs. 6(c), 7(c), and 9(c)].

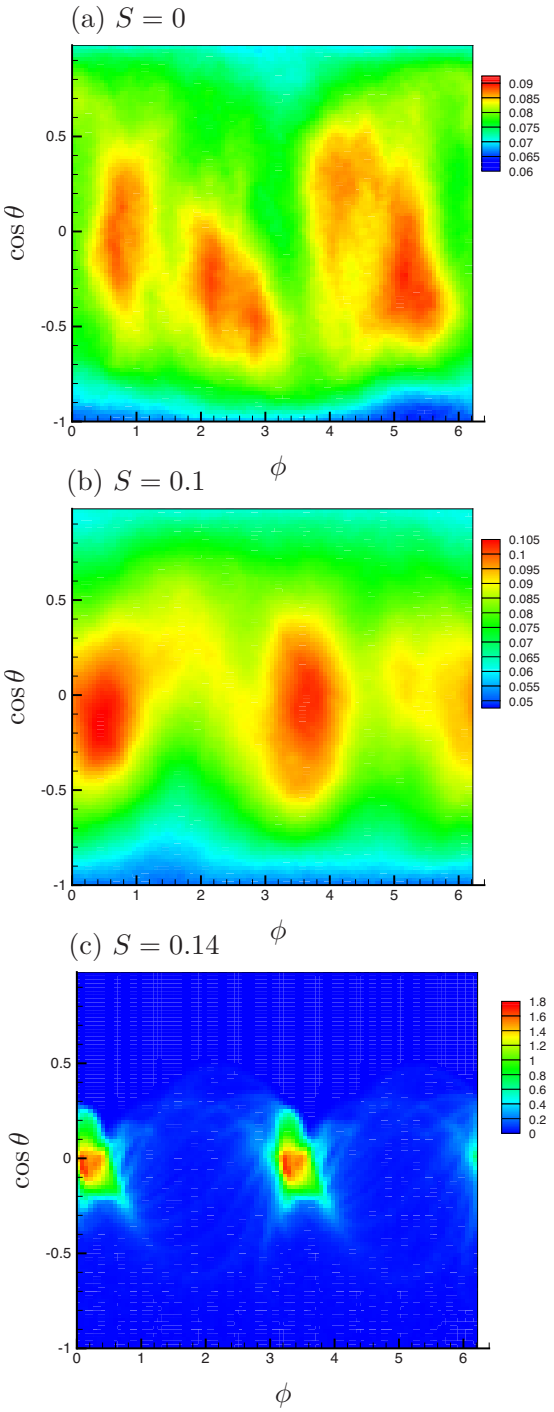

FIG. 12. (Color online) JPDF of the vorticity field for different shear rates: (a) $S=0$ (no imposed flow), (b) $S=0.1$, and (c) $S=0.14$.

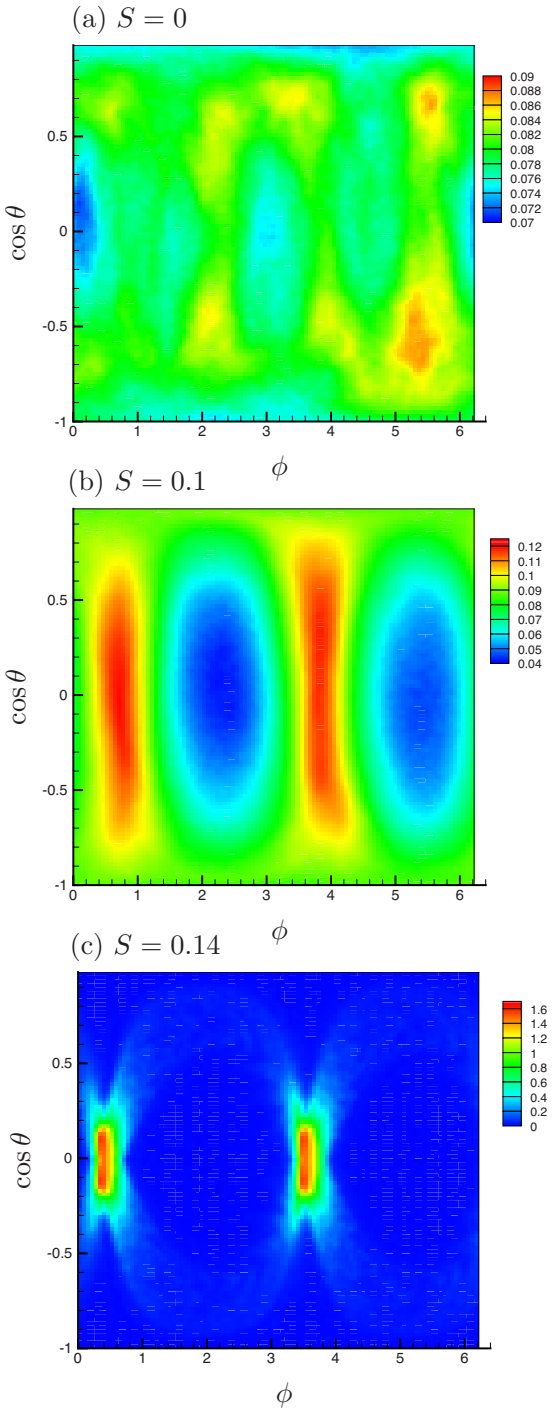

FIG. 13. (Color online) JPDF of the mean director field **n** for different shear rates: (a) $S=0$ (no imposed flow), (b) $S=0.1$, and (c) $S=0.14$.

Finally, the orientation of the particles is characterized in Fig. 13, showing the JPDF of the mean director field $\mathbf{n}(\mathbf{x},t)$ defined in Eq. (13). As expected, particles are oriented isotropically on average when there is no shear flow, and the effect of the flow is to align the particles in the flow direction ($\phi \gtrsim 0$ and π, $\theta = \pi/2$), with a degree of alignment that becomes stronger as the shear rate increases. This effect is not surprising, and is consistent with the base-state orientation distributions obtained in Sec. III B (Fig. 3), and with previous observations made in the absence of hydrodynamic interactions.[46] Comparing this figure with Figs. 11 and 12, a simple picture of the flow is starting to emerge: on average, particles tend to be aligned with and swim in the direction of the flow, which also roughly corresponds to the direction of vortex tubes and of density patterns. This description is however simplistic as these orientation statistics are spatially and temporally averaged.

D. Alignment with rate-of-strain eigenvectors

To gain a more thorough understanding of the flow, we also consider the local alignment of the density and flow

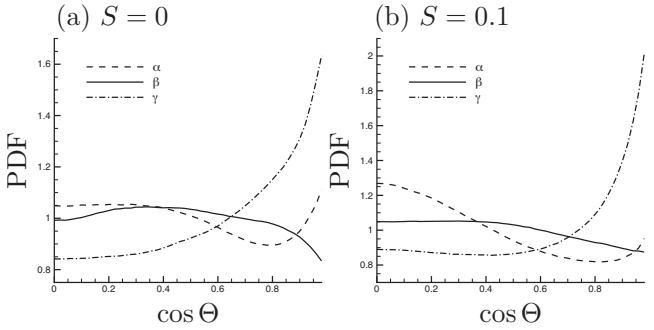

FIG. 14. Probability distribution functions of cos Θ, where Θ denotes the angle between the concentration gradient and the various eigenvectors of the local rate-of-strain tensor, for different shear rates: (a) $S=0$ (no imposed flow) and (b) $S=0.1$.

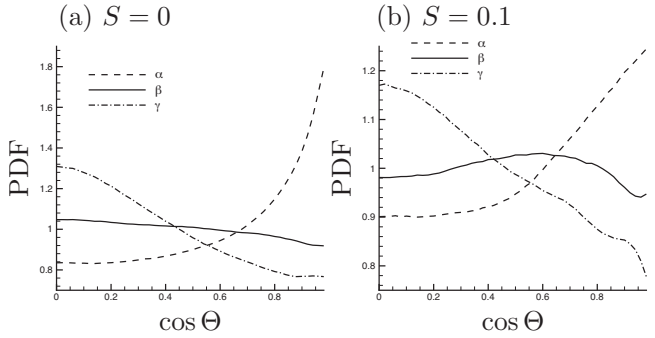

FIG. 16. Probability distribution functions of cos Θ, where Θ denotes the angle between the mean director field and the various eigenvectors of the local rate-of-strain tensor, for different shear rates: (a) $S=0$ (no imposed flow) and (b) $S=0.1$.

structures with respect to the eigenvectors of the disturbance rate-of-strain tensor. We index these eigenvectors by their corresponding eigenvalues α, β, and γ, with $\alpha \geq \beta \geq \gamma$ and $\alpha+\beta+\gamma=0$ owing to incompressibility (see Sec. IV F and Fig. 22 for a discussion of these eigenvalues).

Figure 14 shows probability distribution functions of the cosine of the angle between the directions of the concentration gradient ∇c and of the various eigenvectors of the disturbance rate-of-strain tensor. Both plots for $S=0$ and $S=0.1$ look qualitatively similar, and show a strong alignment of the concentration gradient with the third eigenvector with eigenvalue $\gamma \leq 0$, which corresponds to the local axis of compression of the flow. This suggests that compression by the disturbance flow contributes to the growth of concentration fluctuations in the suspension by advecting particles toward the regions of high density. This correlation between the density gradient and the direction of compression has previously been noted in other unrelated studies involving the dynamics of passive scalar fields in turbulent flows.[68,69]

A similar probability distribution function is shown in Fig. 15 for the angle between the vorticity direction and various rate-of-strain eigenvectors. In this case, alignment with the intermediate eigenvector (with eigenvalue β) is observed for both $S=0$ and $S=0.1$. While this alignment is very good in the absence of flow [$S=0$, Fig. 15(a)], it is less strong when the shear flow is applied [$S=0.1$, Fig. 15(b)], where a peak at $\cos\Theta \approx 0.8$ is observed and suggests an angle of approximately $3\pi/16$ between the vorticity and second eigenvector. This alignment of vorticity with the second strain-rate eigenvector is also commonly observed in simulations of turbulent flows, where it is often considered a universal feature of the flow.[68,69]

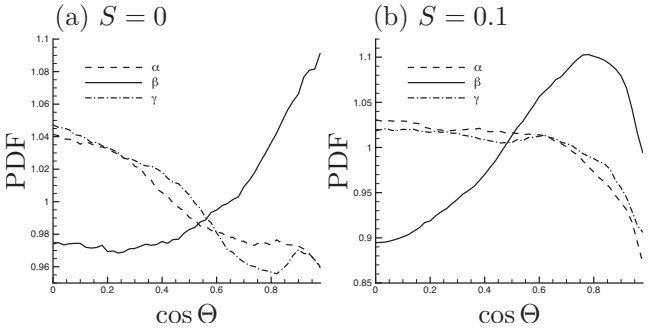

FIG. 15. Probability distribution functions of cos Θ, where Θ denotes the angle between the vorticity vector and the various eigenvectors of the local rate-of-strain tensor, for different shear rates: (a) $S=0$ (no imposed flow) and (b) $S=0.1$.

Finally, the alignment of the mean director field **n** with the rate-of-strain eigenvectors is considered in Fig. 16. The director field is observed to be strongly aligned in the direction of the eigenvector with largest eigenvalue $\alpha \geq 0$, which is also the axis of maximum extension of the disturbance flow. It is also found to align normally with respect to the axis of compression. These effects were to be expected and are a simple consequence of Jeffery's Eq. (4) for the orientational dynamics of the particles, which tend to align particles along the axis of extension in strain-dominated flows.[45]

The data of Figs. 14–16 suggest the following picture for the flow: density patterns (sheets or tubes) tend to align with the axis of maximum extension of the disturbance flow (corresponding to eigenvalue α), which is the combined result of compression by the flow in the direction of the γ-eigenvector and stretching in the direction of the α-eigenvector. In addition, the particles also tend to align with the axis of maximum extension as a direct consequence of Jeffery's Eq. (4), so that they preferably swim along the axis of the density patterns. The vorticity, however, appears to be aligned with the intermediate eigenvector, which, we speculate, might play a role in the destabilization and eventual breakup of the density structures as observed in the dynamics (Fig. 6 and accompanying online movie).

E. Autocorrelation functions

Information about the characteristic size and orientation of the structures can also be obtained from the autocorrelation functions of various flow variables. Figure 17 shows the time-averaged autocorrelation function of the concentration field in the shear plane (x-y plane) for different values of the shear rate S, defined as

$$C_{cc}(\Delta x,\Delta y) = \langle c(x+\Delta x, y+\Delta y, z, t)c(x,y,z,t)\rangle, \qquad (38)$$

where $\langle\cdot\rangle$ denotes a spatial and time-average (after statistical steady state has been reached). When there is no external flow [$S=0$, Fig. 17(a)], the autocorrelation function is isotro-

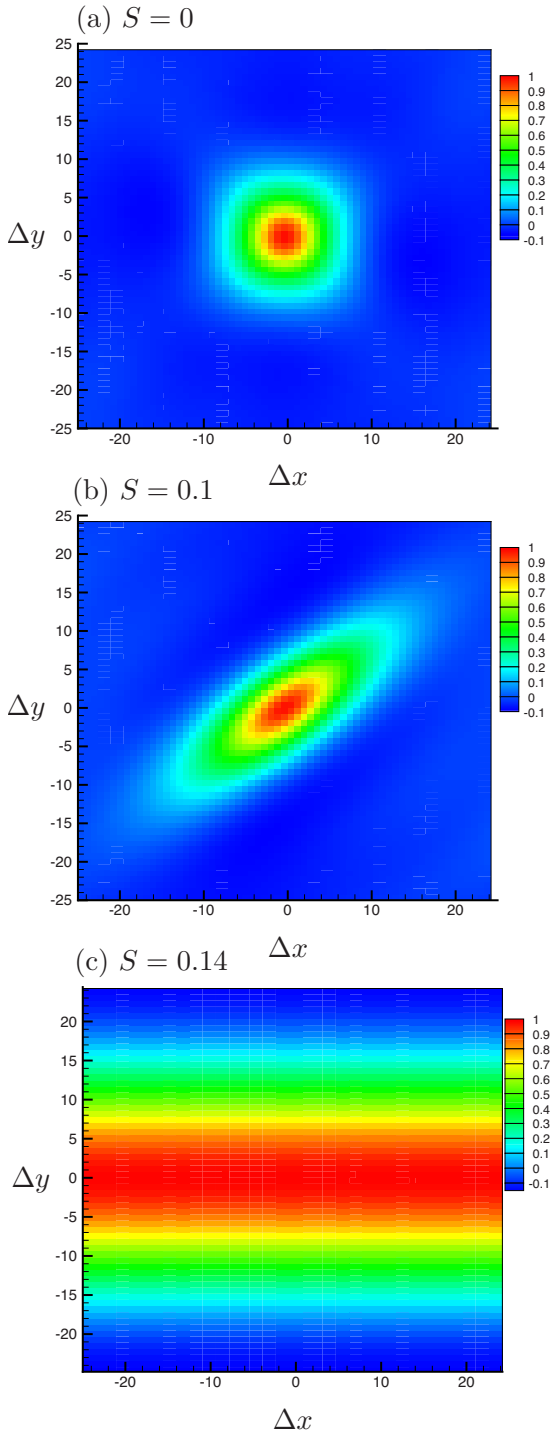

FIG. 17. (Color online) Time-averaged autocorrelation function $C_{cc}(\Delta x, \Delta y)$ of the concentration field in the shear plane (x-y plane) for different shear rates: (a) $S=0$ (no shear flow), (b) $S=0.1$, and (c) $S=0.14$.

pic as expected, as the density patterns have no preferred direction [Fig. 6(a)]. The concentration field exhibits a relatively large correlation length of the order of a quarter of the simulation box size. When a weak shear flow is applied [$S=0.1$, Fig. 17(b)], the flow aligns and stretches the structures along its axis of maximum extension ($\phi=\pi/4$), and correspondingly the concentration field exhibits an anisotropic autocorrelation function, with a longer correlation length along the direction of alignment. After the transition

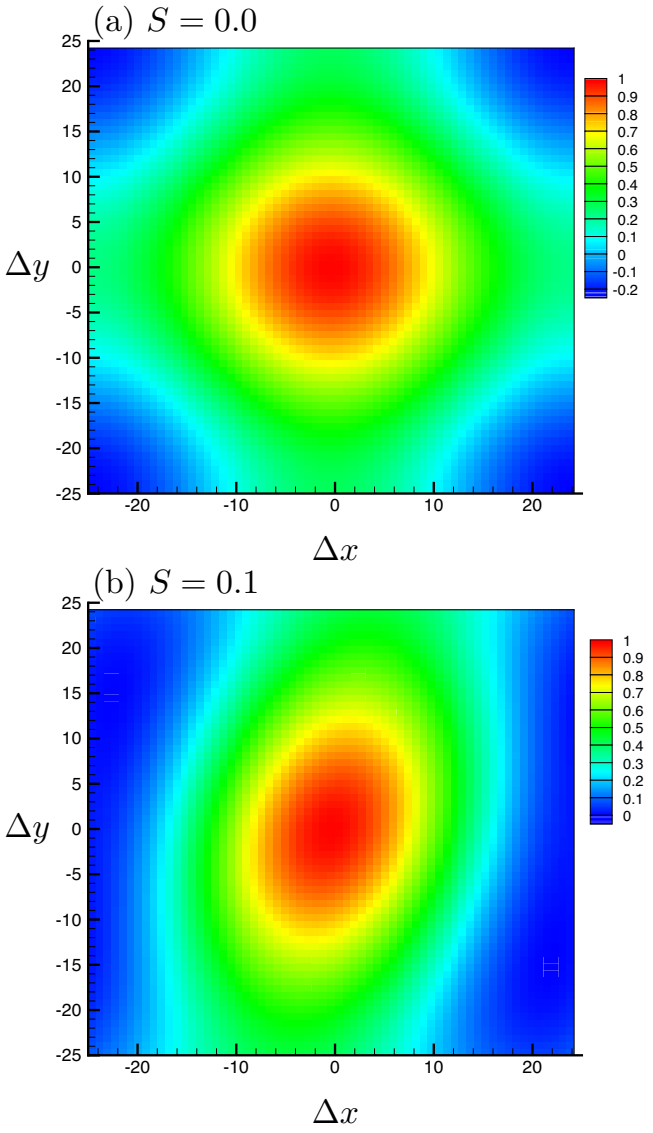

FIG. 18. (Color online) Time-averaged autocorrelation function $C_{uu}(\Delta x, \Delta y)$ of the disturbance velocity field in the shear plane (x-y plane) for different shear rates: (a) $S=0$ (no shear flow) and (b) $S=0.1$.

to two-dimensional instabilities [$S=0.14$, Fig. 17(c)], density fluctuations in the flow direction are suppressed, and the concentration field therefore does not decorrelate in the x-direction. Along the y-direction, it exhibits a long correlation length of the order of half of the domain size.

Qualitatively similar observations can be made on the disturbance velocity field and particle director field, whose autocorrelation functions we define as

$$C_{uu}(\Delta x, \Delta y) = \frac{\langle \mathbf{u}(x+\Delta x, y+\Delta y, z, t) \cdot \mathbf{u}(x, y, z, t) \rangle}{\langle |\mathbf{u}(x, y, z, t)|^2 \rangle}, \quad (39)$$

$$C_{nn}(\Delta x, \Delta y) = \frac{\langle \mathbf{n}(x+\Delta x, y+\Delta y, z, t) \cdot \mathbf{n}(x, y, z, t) \rangle}{\langle |\mathbf{n}(x, y, z, t)|^2 \rangle}. \quad (40)$$

In the case of the velocity field (Fig. 18), the correlation lengths are found to be greater than for the concentration field, and are of the order of the domain size in the absence

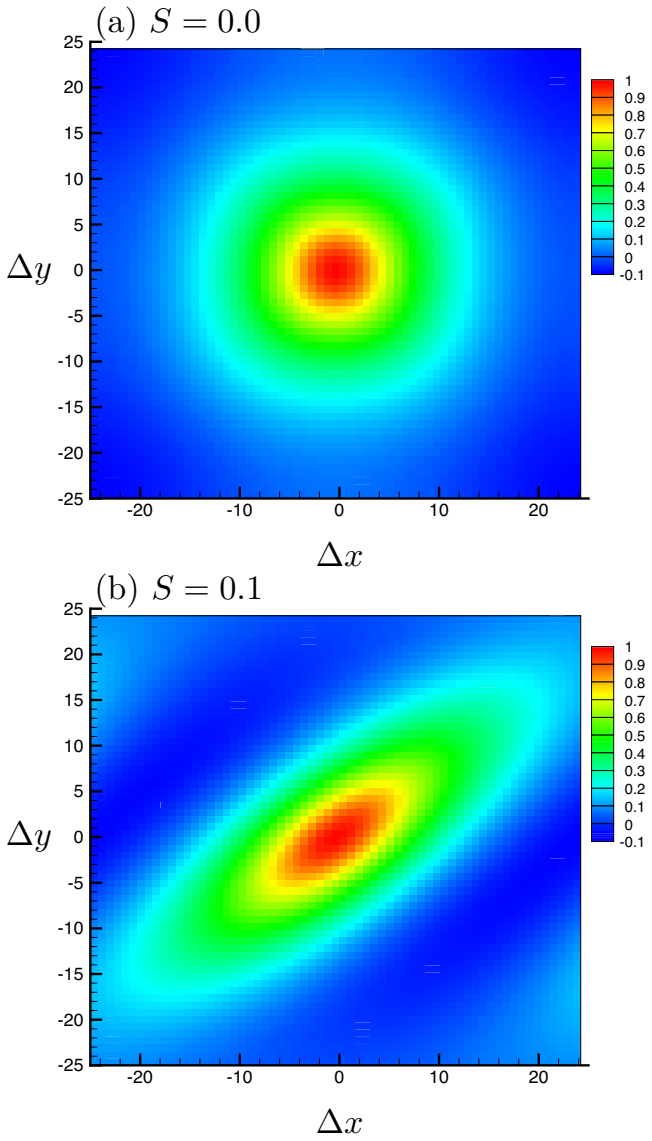

FIG. 19. (Color online) Time-averaged autocorrelation function $C_{nn}(\Delta x, \Delta y)$ of the particle director field in the shear plane (x-y plane) for different shear rates: (a) S=0 (no shear flow) and (b) S=0.1.

of flow [S=0, Fig. 18(a)], in agreement with our previous observations of Sec. IV B 2. At S=0.1 [Fig. 18(b)], the disturbance velocity field is found to decorrelate more rapidly along the flow direction than in the perpendicular directions, although the alignment with the external flow is not as clear as for the concentration field. Figure 19 shows similar data for the particle director field, which is found to follow the exact same trends as the concentration field in Fig. 17, although with slightly larger correlation lengths of the order of half of the domain size.

F. Time dynamics

We finish by presenting a few results on the time dynamics in the suspensions. We first consider the active power input generated by the swimming particles in the flow, which is defined as[30,45]

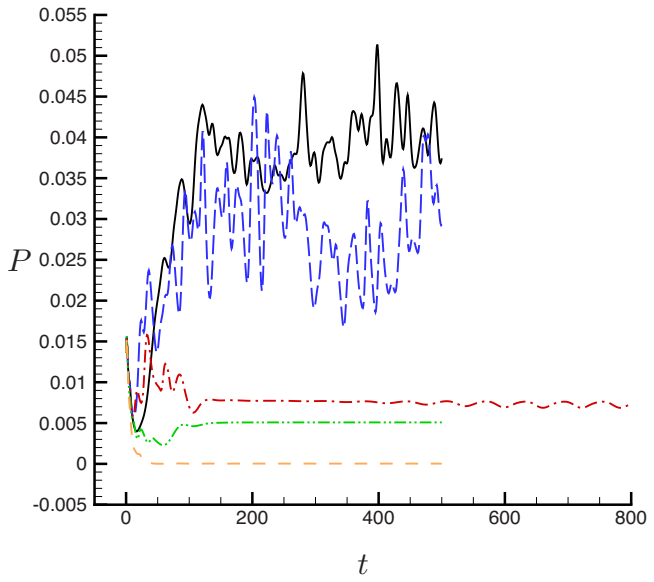

FIG. 20. (Color online) Active power input [Eq. (41)] generated by the swimming particles as a function of time for different shear rates. Solid line ——: S=0, long-dashed line – – –: S=0.1, dash-dotted line –·–: S=0.14, dash-dot-dotted line –·· –: S=0.2, and dashed line - - - -: S=0.3.

$$P(t) = -\alpha \int_V \int_\Omega (\mathbf{pp}:\mathsf{E})\Psi(\mathbf{x},\mathbf{p},t)d\mathbf{p}d\mathbf{x}. \tag{41}$$

Figure 20 shows the time evolution of $P(t)$ in the simulations for various imposed shear rates. In the absence of shear flow (S=0), $P(t)$ starts from a low value corresponding to the random initial configuration of Eq. (31), and quickly increases with time to reach a statistical steady state at a comparatively high value of 0.04. It then fluctuates around this value owing to the unsteadiness of the dynamics. This increase followed by a plateau is consistent with the observations of Saintillan and Shelley[30] in two dimensions, and was expected as the power injected by the swimming particles into the fluid is what drives the instabilities and disturbance flows in the suspensions. As the shear rate increases slightly (S=0.1), the evolution of $P(t)$ remains qualitatively similar, although the value of the plateau is slightly lower than in the absence of shear, which is consistent with a stabilizing effect by the imposed flow. Above the transition to two-dimensional instabilities (S=0.14), the dynamics change drastically: the power input reaches a much lower plateau, and only fluctuates weakly as demonstrated by the weak and slow oscillations observed at long times. The value of $P(t)$ is further reduced after the transition to one-dimensional instabilities (S=0.2), and $P(t)$ quickly decays to zero at higher shear rates when the suspensions are completely stabilized (S=0.3).

A very interesting consequence of the instabilities and disturbance flows analyzed here is that they result in an enhancement of the effective swimming speed of the microorganisms in the case of pushers. This observation was previously made in particle simulations[27] as well as two-dimensional kinetic simulations,[29,30] and is consistent with experimental observations on dense bacterial suspensions where velocities greatly exceeding the single swimmer speed

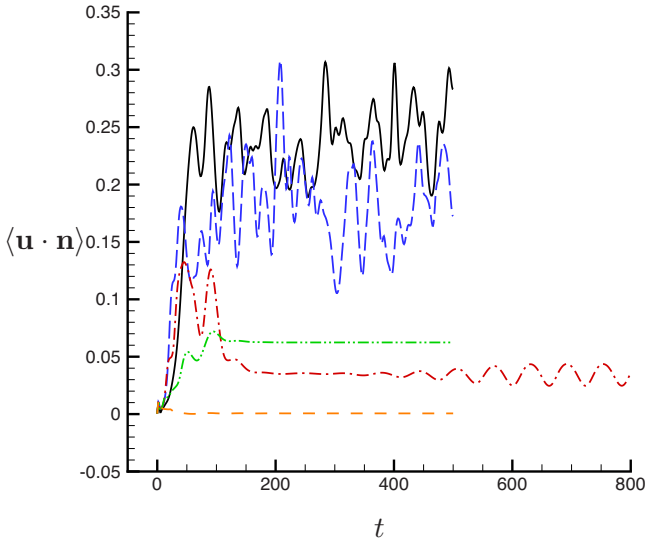

FIG. 21. (Color online) Spatially averaged contraction of the disturbance velocity and director fields $\langle \mathbf{u}\cdot\mathbf{n}\rangle$ [Eq. (42)] as a function of time for different shear rates. Solid line ——: $S=0$, long-dashed line – – –: $S=0.1$, dash-dotted line –·–: $S=0.14$, dash-dot-dotted line –··–: $S=0.2$, and dashed line - - - -: $S=0.3$.

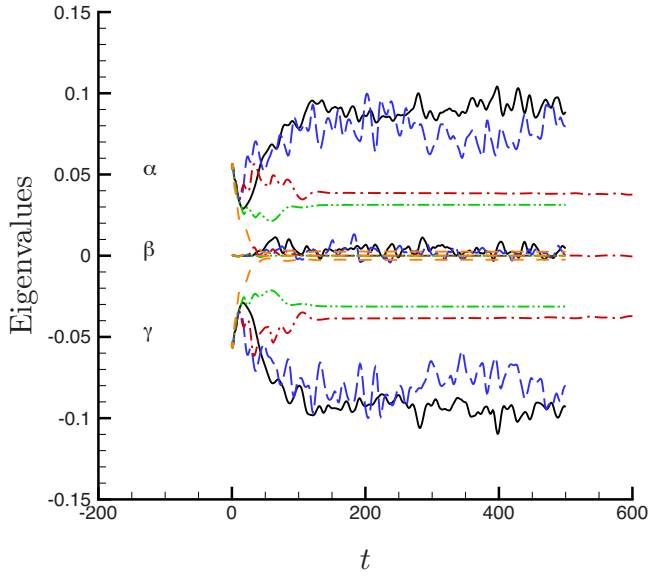

FIG. 22. (Color online) Time evolution of the eigenvalues α, β, and γ of the disturbance rate-of-strain tensor for different imposed shear rates. Solid lines ——: $S=0$, long-dashed lines – – –: $S=0.1$, dash-dotted lines –·–: $S=0.14$, dash-dot-dotted lines –··–: $S=0.2$, and dashed lines - - - -: $S=0.3$.

have been reported.[13,14] To quantify the influence of the external flow on this effect, we consider in Fig. 21 the contraction of the local disturbance velocity $\mathbf{u}(\mathbf{x},t)$ with the director field $\mathbf{n}(\mathbf{x},t)$, which we define after Saintillan and Shelley[30] as

$$\langle \mathbf{u}\cdot\mathbf{n}\rangle(t)=\frac{1}{V}\int_V c(\mathbf{x},t)\mathbf{u}(\mathbf{x},t)\cdot\mathbf{n}(\mathbf{x},t)d\mathbf{x}. \tag{42}$$

The time evolution in the absence of shear flow ($S=0$) is consistent with the two-dimensional simulations of Saintillan and Shelley,[30] and exhibits an increase of $\langle \mathbf{u}\cdot\mathbf{n}\rangle$ from zero to a positive plateau of approximately 0.20 as the instabilities start to develop. This suggests again that the particles tend to align locally with the disturbance flow, a direct consequence of Jeffery's Eq. (4), and that this local alignment is polar and in the direction of the disturbance velocity. This indeed corresponds to an effective enhancement of the mean particle swimming speed as a result of mean-field hydrodynamic interactions via the disturbance flow. This alignment is less pronounced when a shear flow is applied, as demonstrated by lower plateaus reached by $\langle \mathbf{u}\cdot\mathbf{n}\rangle$ as S increases. Finally, $\langle \mathbf{u}\cdot\mathbf{n}\rangle=0$ in the fully stable case ($S=0.3$), i.e., no enhancement occurs. These observations all confirm that the instabilities that arise in suspensions of pushers play a critical role in the enhancement of particle velocities reported in experiments.[13]

Finally, Fig. 22 presents data on the eigenvalues of the disturbance rate-of-strain tensor, whose role we analyzed earlier in Sec. IV D. For all flow rates, we find that the first and third eigenvalues α and γ, which are respectively, positive and negative, have similar magnitudes. The intermediate eigenvalue β is of very small magnitude at low shear rates and fluctuates around zero, although with a small positive mean; it becomes exactly zero above the transition to two-dimensional instabilities. As the instabilities take place, the magnitudes of α and γ both increase to reach plateau values. The effect of the shear flow, as expected, is to decrease these steady-state values as a result of the damping of the instabilities. When the flow is fully stabilized by the imposed shear ($S=0.3$), all three eigenvalues quickly decay to zero.

V. SUMMARY

We have presented a theoretical and computational study of the effects of an externally imposed simple shear flow on the dynamics in dilute suspensions of swimming microorganisms. The study was based on the previous kinetic model proposed by Saintillan and Shelley,[29,30] which represents a suspension of self-propelled particles by means of a probability distribution function for the particle positions and orientations, which evolve as a result of single particle swimming, translational and angular diffusions, and translation and rotation under the local flow field. This flow field is decomposed as the sum of the imposed shear flow and of the disturbance flow induced by the individual force dipoles exerted by the particles on the fluid as they swim.

Using this kinetic model, we first performed a linear stability analysis, which demonstrates that the main effect of the shear flow is to stabilize the instabilities that occur when no flow is applied. We confirmed this prediction by performing large-scale three-dimensional simulations of the kinetic equations using an efficient parallel spectral code and Rogallo's classic method[57] to account for the external flow. These simulations indeed demonstrated the stabilizing effect of the shear flow. Furthermore, we found that this stabilization is direction-dependent and occurs first in the flow direction, followed by the gradient direction, and eventually by the direction perpendicular to the shear plane, as demonstrated by transitions from three- to two- to one-dimensional instabilities, followed by an eventual stabilization of the flow as the imposed shear rate increases. In addition, these nonlinear simulations were also used to characterize the density pat-

terns and complex flow fields that arise in the suspensions at long time. These flows were found to be strongly chaotic and reminiscent of high-Reynolds-number turbulence. While some specific characteristics of the flows were found to be similar to turbulence, and in particular the shape of Q-R plots and the alignment of the vorticity vector with the intermediate strain-rate eigenvector, other features differed significantly, notably the very strong predominance of large scales in the present simulations.

As discussed in Sec. I, one application of the present study lies in the effective rheology of suspensions of self-propelled particles. Previous theoretical models[42–47] have analyzed the rheology of very dilute suspensions by completely neglecting the effects of particle-particle interactions (even in the mean-field sense). These studies have found that suspensions of self-propelled particles should exhibit decreased viscosities in the case of pushers, but increased viscosities for pullers, in qualitative agreement with experiments.[41,70] These conclusions assumed homogeneous suspensions with steady orientation distributions: the present work suggests that at low shear rates the instabilities that occur as a result of interactions will modify, at least quantitatively, the results of these previous dilute theories. The precise effects of these instabilities on the rheology remain to be analyzed and will be the subject of future work.

ACKNOWLEDGMENTS

The authors thank Michael Shelley (Courant Institute) for useful conversations on this work, and gratefully acknowledge funding from NSF Grant No. DMS-0920931-ARRA. Computer resources were provided by the National Center for Supercomputing Applications (NCSA) at the University of Illinois.

[1]E. M. Purcell, "Life at low Reynolds number," Am. J. Phys. **45**, 3 (1977).
[2]C. Brennen and H. Winet, "Fluid mechanics of propulsion by cilia and flagella," Annu. Rev. Fluid Mech. **9**, 339 (1977).
[3]E. Lauga and T. R. Powers, "The hydrodynamics of swimming microorganisms," Rep. Prog. Phys. **72**, 096601 (2009).
[4]S. J. Ebbens and J. R. Howse, "In pursuit of propulsion at the nanoscale," Soft Matter **6**, 726 (2010).
[5]W. F. Paxton, K. C. Kistler, C. C. Olmeda, A. Sen, S. K. St. Angelo, Y. Cao, T. E. Mallouk, P. E. Lammert, and V. H. Crespi, "Catalytic nanomotors: Autonomous movement of striped nanorods," J. Am. Chem. Soc. **126**, 13424 (2004).
[6]W. F. Paxton, A. Sen, and T. E. Mallouk, "Motility of catalytic nanoparticles through self-generated forces," Chem.-Eur. J. **11**, 6462 (2005).
[7]J. R. Howse, R. A. L. Jones, A. J. Ryan, T. Gough, R. Vafabakhsh, and R. Golestanian, "Self-motile colloidal particles: From directed propulsion to random walk," Phys. Rev. Lett. **99**, 048102 (2007).
[8]J. L. Moran, P. M. Wheat, and J. D. Posner, "Locomotion of electrocatalytic nanomotors due to reaction induced charge autoelectrophoresis," Phys. Rev. E **81**, 065302 (2010).
[9]J. G. Gibbs and Y.-P. Zhao, "Design and characterization of rotational multicomponent catalytic nanomotors," Small **5**, 2304 (2009).
[10]T. Ishikawa, "Suspension biomechanics of swimming microbes," J. R. Soc., Interface **6**, 815 (2009).
[11]S. Ramaswamy, "The mechanics and statistics of active matter," Condens. Matter Phys. **1**, 323 (2010).
[12]D. L. Koch and G. Subramanian, "Collective hydrodynamics of swimming micro-organisms: Living fluids," Annu. Rev. Fluid Mech. **43**, 637 (2011).
[13]C. Dombrowski, L. Cisneros, S. Chatkaew, R. E. Goldstein, and J. O. Kessler, "Self-concentration and large-scale coherence in bacterial dynamics," Phys. Rev. Lett. **93**, 098103 (2004).
[14]L. H. Cisneros, R. Cortez, C. Dombrowski, R. E. Goldstein, and J. O. Kessler, "Fluid dynamics of self-propelled micro-organisms, from individuals to concentrated populations," Exp. Fluids **43**, 737 (2007).
[15]N. H. Mendelson, A. Bourque, K. Wilkening, K. R. Anderson, and J. C. Watkins, "Organized cell swimming motions in *Bacilus subtilis* colonies: Patterns of short-lived whirls and jets," J. Bacteriol. **181**, 600 (1999).
[16]A. Sokolov, I. S. Aranson, J. O. Kessler, and R. E. Goldstein, "Concentration dependence of the collective dynamics of swimming bacteria," Phys. Rev. Lett. **98**, 158102 (2007).
[17]G. V. Soni, B. M. Jaffar Ali, Y. Hatwalne, and G. V. Shivashankar, "Single particle tracking of correlated bacterial dynamics," Biophys. J. **84**, 2634 (2003).
[18]X.-L. Wu and A. Libchaber, "Particle diffusion in a quasitwo-dimensional bacterial bath," Phys. Rev. Lett. **84**, 3017 (2000).
[19]M. J. Kim and K. S. Breuer, "Enhanced diffusion due to motile bacteria," Phys. Fluids **16**, L78 (2004).
[20]K. C. Leptos, J. S. Guasto, J. P. Gollub, A. I. Pesci, and R. E. Goldstein, "Dynamics of enhanced tracer diffusion in suspensions of swimming eukaryotic micro-organisms," Phys. Rev. Lett. **103**, 198103 (2009).
[21]Q. Liao, G. Subramanian, M. P. DeLisa, D. L. Koch, and M. Wu, "Pair velocity correlations among swimming Escherichia coli bacteria are determined by force-quadrupole hydrodynamic interactions," Phys. Fluids **19**, 061701 (2007).
[22]J. P. Hernández-Ortiz, C. G. Stoltz, and M. D. Graham, "Transport and collective dynamics in suspensions of confined self-propelled particles," Phys. Rev. Lett. **95**, 204501 (2005).
[23]J. P. Hernández-Ortiz, P. T. Underhill, and M. D. Graham, "Dynamics of confined suspensions fo swimming particles," J. Phys.: Condens. Matter **21**, 204107 (2009).
[24]T. Ishikawa and T. J. Pedley, "Diffusion of swimming model microorganisms in a semidilute suspensions," J. Fluid Mech. **588**, 437 (2007).
[25]T. Ishikawa, J. T. Locsei, and T. J. Pedley, "Development of coherent structures in concentrated suspensions of swimming model microorganisms," J. Fluid Mech. **615**, 401 (2008).
[26]A. Kanevsky, M. J. Shelley, and A.-K. Tornberg, "Modeling simple locomotors in Stokes flow," J. Comput. Phys. **229**, 958 (2010).
[27]D. Saintillan and M. J. Shelley, "Orientational order and instabilities in suspensions of self-locomoting rods," Phys. Rev. Lett. **99**, 058102 (2007).
[28]R. Aditi Simha and S. Ramaswamy, "Hydrodynamic fluctuations and instabilities in ordered suspensions of self-propelled particles," Phys. Rev. Lett. **89**, 058101 (2002).
[29]D. Saintillan and M. J. Shelley, "Instabilities and pattern formation in active particle suspensions: Kinetic theory and continuum simulations," Phys. Rev. Lett. **100**, 178103 (2008).
[30]D. Saintillan and M. J. Shelley, "Instabilities, pattern formation, and mixing in active suspensions," Phys. Fluids **20**, 123304 (2008).
[31]C. Hohenegger and M. J. Shelley, "Stability of active suspensions," Phys. Rev. E **81**, 046311 (2010).
[32]I. S. Aranson, A. Sokolov, J. O. Kessler, and R. E. Goldstein, "Model for dynamical coherence in thin films of self-propelled micro-organisms," Phys. Rev. E **75**, 040901 (2007).
[33]G. Subramanian and D. L. Koch, "Critical bacterial concentration for the onset of collective swimming," J. Fluid Mech. **632**, 359 (2009).
[34]A. Baskaran and M. C. Marchetti, "Hydrodynamics of self-propelled hard rods," Phys. Rev. E **77**, 011920 (2008).
[35]A. Baskaran and M. C. Marchetti, "Statistical mechanics and hydrodynamic of bacterial suspensions," Proc. Natl. Acad. Sci. U.S.A. **106**, 15567 (2009).
[36]S. Mishra, A. Baskaran, and M. C. Marchetti, "Fluctuations and pattern formation in self-propelled particles," Phys. Rev. E **81**, 061916 (2010).
[37]T. J. Pedley, "Instability of uniform micro-organism suspensions revisited," J. Fluid Mech. **647**, 335 (2010).
[38]F. Peters, C. Marrase, H. Havskum, F. Rassoulzadegan, J. Dolan, M. Alcaraz, and J. M. Gasol, "Turbulence and the microbial food web: Effects on bacterial losses to predation and on community structure," J. Plankton Res. **24**, 321 (2002).
[39]Marcos and R. Stocker, "Micro-organisms in vortices: A microfluidic setup," Limnol. Oceanogr. **4**, 392 (2006).
[40]W. Durham, J. O. Kessler, and R. Stocker, "Disruption of motility by shear triggers formation of thin phytoplankton layers," Science **323**, 1067 (2009).
[41]A. Sokolov and I. S. Aranson, "Reduction of viscosity in suspension of swimming bacteria," Phys. Rev. Lett. **103**, 148101 (2009).
[42]Y. Hatwalne, S. Ramaswamy, M. Rao, and R. Aditi Simha, "Rheology of

active-particle suspensions," Phys. Rev. Lett. **92**, 118101 (2004).
[43]B. M. Haines, I. S. Aranson, L. Berlyand, and D. A. Karpeev, "Effective viscosity of dilute bacterial suspensions: A two-dimensional model," Phys. Biol. **5**, 046003 (2008).
[44]B. M. Haines, A. Sokolov, I. S. Aranson, L. Berlyand, and D. A. Karpeev, "Three-dimensional model for the effective viscosity of bacterial suspensions," Phys. Rev. E **80**, 041922 (2009).
[45]D. Saintillan, "Extensional rheology of active suspensions," Phys. Rev. E **81**, 056307 (2010).
[46]D. Saintillan, "The dilute rheology of swimming suspensions: A simple kinetic model," Exp. Mech. **50**, 1275 (2010).
[47]L. Giomi, T. B. Liverpool, and M. C. Marchetti, "Sheared active fluids: Thickening, thinning, and vanishing viscosity," Phys. Rev. E **81**, 051908 (2010).
[48]M. Doi and S. F. Edwards, *The Theory of Polymer Dynamics* (Oxford University Press, Oxford, 1986).
[49]F. P. Bretherton, "The motion of rigid particles in a shear flow at low Reynolds number," J. Fluid Mech. **14**, 284 (1962).
[50]G. K. Batchelor, "Transport properties of two-phase materials with random structures," Annu. Rev. Fluid Mech. **6**, 227 (1974).
[51]E. J. Hinch and L. G. Leal, "Constitutive equations in suspension mechanics. Part 1. General formulation," J. Fluid Mech. **71**, 481 (1975).
[52]G. K. Batchelor, "The stress generated in a nondilute suspension of elongated particles by pure straining motion," J. Fluid Mech. **46**, 813 (1971).
[53]E. J. Hinch and L. G. Leal, "Constitutive equations in suspension mechanics. Part 2. Approximate forms for a suspension of rigid particles affected by Brownian rotations," J. Fluid Mech. **76**, 187 (1976).
[54]S. B. Chen and L. Jiang, "Orientation distribution in a dilute suspension of fibers subject to simple shear flow," Phys. Fluids **11**, 2878 (1999).
[55]S. B. Chen and D. L. Koch, "Rheology of dilute suspensions of charged fibers," Phys. Fluids **8**, 2792 (1996).
[56]B. D. Hoffman and E. S. G. Shaqfeh, "The effect of Brownian motion on the stability of sedimenting suspensions of polarizable rods in an electric field," J. Fluid Mech. **624**, 361 (2009).
[57]R. Rogallo, "Numerical experiments in homogeneous turbulence," NASA Tech. Memo. **176**, 81315 (1981).
[58]M. M. Rogers and P. Moin, "The structure of the vorticity field in homogeneous turbulent flows," J. Fluid Mech. **176**, 33 (1987).
[59]A. W. Lees and S. F. Edwards, "The computer study of transport processes under extreme conditions," J. Phys. C **5**, 1921 (1972).
[60]H. Hasimoto, "On the periodic fundamental solutions of the Stokes equations and their application to viscous flow pas a cubic array of spheres," J. Fluid Mech. **5**, 317 (1959).
[61]D. Saintillan and M. J. Shelley, personal communication (9 October 2010).
[62]J. C. Hunt, A. A. Wray, and P. Moin, "Eddies, stream, and convergence zones in turbulent flows," Center for Turbulence Research Report, CTR S88, 193 (1988).
[63]M. S. Chong, A. E. Perry, and B. J. Cantwell, "A general classification of three-dimensional flow fields," Phys. Fluids A **2**, 765 (1990).
[64]J. Jeong and F. Hussain, "On the identification of a vortex," J. Fluid Mech. **285**, 69 (1995).
[65]H. M. Blackburn, N. M. Mansour, and B. J. Cantwell, "Topology of fine-scale motions in turbulent channel flow," J. Fluid Mech. **310**, 269 (1996).
[66]J. Soria, R. Sondergaard, B. J. Cantwell, M. S. Chong, and A. E. Perry, "A study of fine-scale motions of incompressible time-developing mixing layers," Phys. Fluids **6**, 871 (1994).
[67]J. M. Chacin and B. J. Cantwell, "Dynamics of a low Reynolds number turbulent boundary layer," J. Fluid Mech. **404**, 87 (2000).
[68]J. M. Wallace, "Twenty years of experimental and direct numerical simulation access to the velocity gradient tensor: What have we learned about turbulence?" Phys. Fluids **21**, 021301 (2009).
[69]W. T. Ashurst, A. R. Kerstein, R. M. Kerr, and C. H. Gibson, "Alignment of vorticity and scalar gradient with strain rate in simulated Navier–Stokes turbulence," Phys. Fluids **30**, 2343 (1987).
[70]S. Rafaï, L. Jibuti, and P. Peyla, "Effective viscosity of micro-swimmer suspensions," Phys. Rev. Lett. **104**, 098102 (2010).